

Article

Agates from Mesoproterozoic Volcanics (Pasha–Ladoga Basin, NW Russia): Characteristics and Proposed Origin

Evgeniya N. Svetova *  and Sergei A. Svetov

Institute of Geology, Karelian Research Centre of RAS, 185910 Petrozavodsk, Russia

* Correspondence: enkotova@rambler.ru

Abstract: Agate gemstones occurring in the Mesoproterozoic volcanic rocks of the Priozersk Formation (PrF) within the Pasha–Ladoga Basin (Fennoscandian Shield, NW Russia) were investigated to characterize the mineral and geochemical composition of the agates and provide new information concerning their origin. Optical and scanning electron microscopy, EDS microanalysis, X-ray powder diffraction, X-ray fluorescence spectrometry, Raman spectroscopy, inductively coupled plasma mass spectrometry (ICP-MS), and C–O isotope analysis were used for the study. Agate mineralization appears mostly as an infill of fissures, cavities, gas vesicles in massive and vesicular basalts, lava-breccias. The mineral composition of agates is dominated by alpha-quartz (fibrous chalcedony, microcrystalline and macrocrystalline quartz), but it also displays abundances of calcite. The characteristic red-brownish agate's coloration is caused by multiple hematite inclusions distributed in an agate matrix. The study revealed the two phases of agate formation in the PrF volcanics, which are most likely controlled by two distinctly different fluids and/or their mixture. At first, agates appeared due to post-magmatic iron-rich fluids. The late hydrothermal activity was probably triggered by intrusion of gabbro-dolerite sill and resulted in the second phase of agate formation. We suggest that the late hydrothermal fluids remobilized the iron compounds from the crust of weathering underlying the PrF volcanics, which led to additional formation of vein agates and filling of gas vesicles with hematite-rich calcite/silica matter.

Keywords: agates; Mesoproterozoic volcanics; Fennoscandia Shield; Raman spectroscopy; X-ray diffraction; SEM-EDS; C–O isotope; genesis



Citation: Svetova, E.N.; Svetov, S.A. Agates from Mesoproterozoic Volcanics (Pasha–Ladoga Basin, NW Russia): Characteristics and Proposed Origin. *Minerals* **2023**, *13*, 62. <https://doi.org/10.3390/min13010062>

Academic Editors: Stefanos Karampelas and Emmanuel Fritsch

Received: 12 December 2022
Revised: 24 December 2022
Accepted: 27 December 2022
Published: 30 December 2022



Copyright: © 2022 by the authors. Licensee MDPI, Basel, Switzerland. This article is an open access article distributed under the terms and conditions of the Creative Commons Attribution (CC BY) license (<https://creativecommons.org/licenses/by/4.0/>).

1. Introduction

Agates belong to the fascinating variety of gemstones that have attracted people's attention since ancient times, owing to the showiness and uniqueness of their patterns. Due to the wide variation in shape, size and colour, agates are of considerable use in stone-cutting art as a valuable decorative and ornamental material. Agates are generally defined as banded or patterned chalcedony that are mainly composed of minute crystals of α -quartz [1]. They usually contain other silica polymorphs (moganite, cristobalite, tridymite, opal-CT) and paragenetic minerals (carbonates, zeolites, clay minerals, iron oxides, etc.) [2]. Agate occurrences are distributed throughout the world and related to various volcanic and, to a lesser extent, sedimentary rocks. Agates ordinarily fill veins and cavities in volcanic rocks where the supply of silica is triggered by post-magmatic hydrothermal activity, combined with the influence of meteoric waters [3,4]. Silica accumulation in cavities and empty pore space of sedimentary rocks often takes place during sedimentation or early diagenesis, when the sediments contain enough moisture [2]. The established agate hosts range in age from 13 to 3480 Ma [5]. The oldest known agate occurrence was found in Western Australia (Warrawoona) within Archean metamorphosed rhyolitic tuffs [6]. Miocene (13 Ma) volcanic tuffs of Yucca mountain, USA, belong to the youngest known agate-bearing host [1].

Agate occurrences on the Southeast Fennoscandia Shield are mainly related with Precambrian mafic volcanic rocks. The oldest famous agate hosts are the Paleoproterozoic massive and pillow lavas of the Ludicovian Superhorizont (ca. 2100–1920 Ma) within the Onega Basin [7,8]. In the present paper, agates from the volcanic rocks of the Mesoproterozoic Pasha–Ladoga Basin (Fennoscandian Shield, NW Russia) were investigated. The occurrence of so-called Salmi agates (after the name of the nearby village) was initially discovered in 1969 during a geologic exploration to the south of Pitkäranta town and later described by Polekhovsky and Punin in 2008 [9]. The study aims to obtain new information concerning the genesis of the Salmi agates. An integrated geological, mineralogical, geochemical, and C-O isotope data provides information for the reconstruction of geological and geochemical processes leading to the agate formation in the volcanics and the interpretation of their mineralogical features.

2. Geological Setting

The Mesoproterozoic Pasha–Ladoga Basin (PLB) is located at the margin of the Archean Karelian Craton and the Paleoproterozoic Svecofenian Belt in northwest Russia (Figure 1) [10–12]. The PLB, with an area of about 70,000 km², is bounded by a northwest-striking faults system. The PLB was formed during the Early Mesoproterozoic rifting.

The PLB rocks with angular unconformity overlay Archean granitoids (2.70–2.66 Ga), Paleoproterozoic hornblende-biotitic gneisses, shales, amphibolites (1.97–1.95 Ga), and metaturbidites (ca. 1.88 Ga) [13], and are intruded by the Salmi anorthosite–gabbro–gapakivi-granite complex (1.55–1.53 Ga) [14,15]. PLB is separated from these Archean and Paleoproterozoic rocks by a horizon of crust of weathering. The crust of weathering with a thickness of 0.5–5 to 30 m has a wide lateral distribution. It was probably formed in a range of 1.53–1.50 Ga and represented by hematized clay-altered basement rocks [16].

The PLB comprises four Mesoproterozoic (Riphean in Russian stratigraphic scale) units (from oldest to youngest): the Priozersk, Salmi, Pasha and Pliladoga, with a total thickness of 430–1250 m and Neoproterozoic (Vendian in Russian stratigraphic scale) Yablonovka Formation with thickness 90–380 m [11] (pp. 145–147), [12]. Volcanics are recognized only in the upper parts of Priozersk, Salmi, and Pasha Formations. The studied PLB area (the northeastern side of basin) is characterized by the following sequences, respectively, [10] (pp. 74–75), [11] (pp. 145–147), [17] (pp. 49–50), [12,18] (Figure 1C):

Priozersk Formation (PrF) comprises terrigenous sedimentary sequence (with a thickness from the first to 450 m) of red-coloured arkose sandstones, mudstones, gravelstones, and conglomerates, underlying the volcanic sequence (with a total thickness of 120 m or more). Volcanics are presented by nine lava flows of basalts interbedded with horizons of tuff, tuff-breccia, tuffites, and sandstones.

Salmi Formation (SalF) with a total thickness of 120–200 m overlies erosion rock layer covering the PrF volcanics. The basement of the PrF sequence is formed by quartz-feldspar and polymictic sandstones, mudstones with thin carbonate interbeds. The sedimentary sequence is overlain by lavas of porphyritic basalt and andesibasalts interbedded with tuffs and tuffites. The thickness of volcanics is about 80 m.

Pasha Formation (PashF) has a total thickness of 150 to 500 m and is represented by coarse-grained feldspar-quartz sandstones and gravelstones with fragments of quartzites. Single lava flows and interlayers of tuffs similar to PrF volcanic rocks were found within the sedimentary sequence. The thickness of the volcanic sequence is about 20 m.

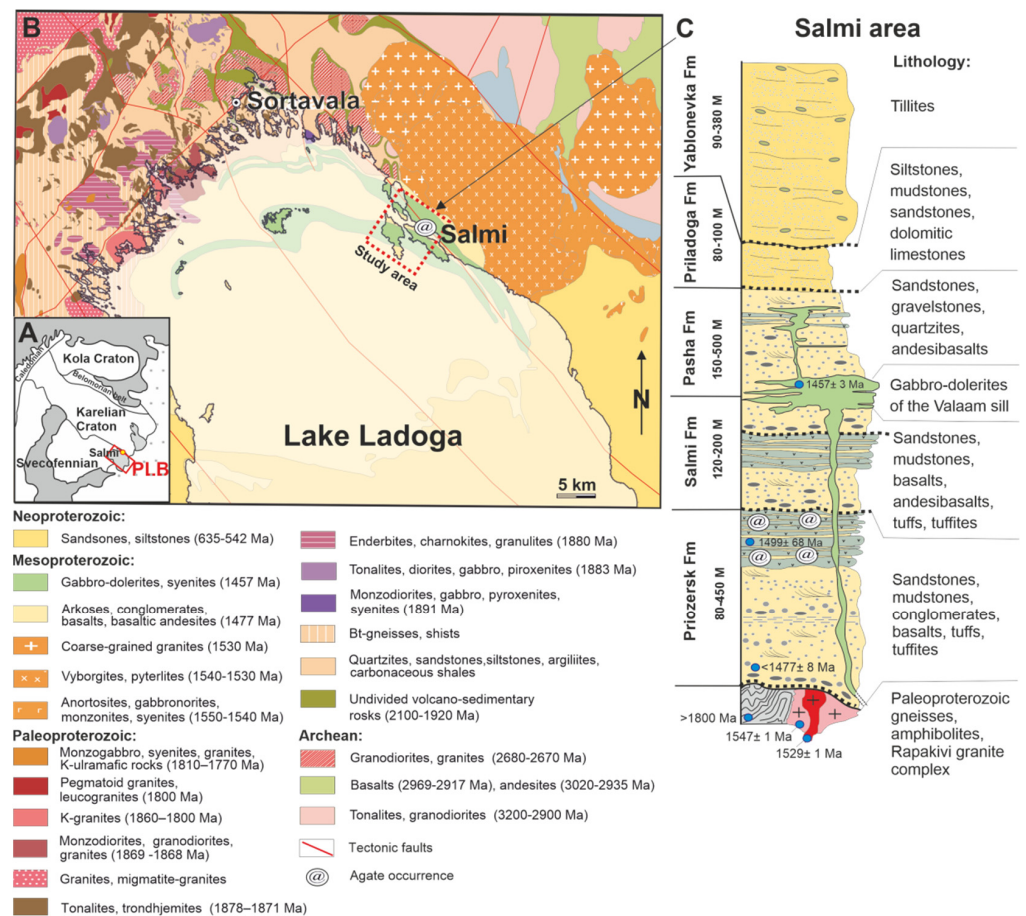


Figure 1. (A) Location of sampling areas. (B) simplified geological map of the Pasha–Ladoga Basin based on [18]. (C) simplified geological section of the studied area based on [12], [17] (pp. 49–50). Dotted line marks position of weathered crusts or erosion rock layers; @ represents sampled agate-bearing flows.

The erosion rock layer developed after the PashF sequence is overlain with rocks of the *Priladoga Formation (PrilF)* formed by thin-layered siltstones, mudstones and fine-medium-grained sandstones, with interlayers of dolomitic limestones in the upper part of the sequence. The total thickness of PrilF is ca. 80–100 m. The PrilF rocks with angular unconformity are overlain by the Neoproterozoic rocks of the *Yablonoška Formation (JabF)*. The JabF sequence has a thickness of 90–380 m and is represented by tillites [17] (p. 49).

The PLB volcanics (observed in PrF, SalF, PashF) age can be comprehensively estimated based on the following data. PrF overlaps the weathered crust of rapakivi granites (Salmi batholith), aged on intrusion phases from 1547 ± 1 to 1529 ± 1 Ma [14]. A depositional age of the PrF volcanics by the Sm/Nd isotopic data is 1499 ± 68 Ma [19]. The U–Pb dating of the youngest detrital zircon from the basal part of the PrF sandstone is ca. 1477 ± 8 Ma [20]. The PrF, SalF, and PashF rocks are intruded by gabbro-dolerites of the Valaam Sill aged 1457 ± 3 Ma and 1459 ± 3 Ma [21]. The data obtained indicates that the dominating part of the PLB (PrF, SalF, PashF) was formed very rapidly in the interval 1477–1457 Ma in the intraplate riftogenic regime [11] (pp. 145–147).

The volcanic-sedimentary complexes of the PLB basement have not undergone regional metamorphism, but were affected to diagenetic and local hydrothermal alterations [12]. The PLB is overlapped by the Vendian and Phanerozoic sediments [11] (pp. 145–147).

3. Agate Occurrence

The studied area is located near the Salmi village, where, in the Tulemajoki River-valley outcrop, bedrock attributed to the upper part of the PrF sequence are recorded. The volcanic sequence with a thickness about of 100 m is exposed in riverbed outcrops (on rapids and rifts). It is represented by interbedded gently dipping massive lava flows of basalts, andesibasalts, and andesites that are 1–30 m in thickness. The lava flows are alternated with slag lavas, agglomerate tuffs, tuffites, tuff sandstones, gravelstones, and small-pebble conglomerates. The thickness of these beds varies from tens of cm to 5 m.

The thick lava flows (>5 m) are differentiated (Figure 2A,B). They are formed by massive rocks with single agate nodules at the flow's base. The middle part of the flows is characterized by porphyritic structure. The number of agate nodules and veinlets increases (it can reach 40% of the volume) towards the upper parts of the lava flows. The top lava flows are formed of breccias or frothy lavas (similar to slags) and contain numerous cavities and gas vesicles partially or completely filled with agates of quartz-carbonate composition (Figure 2C,D).

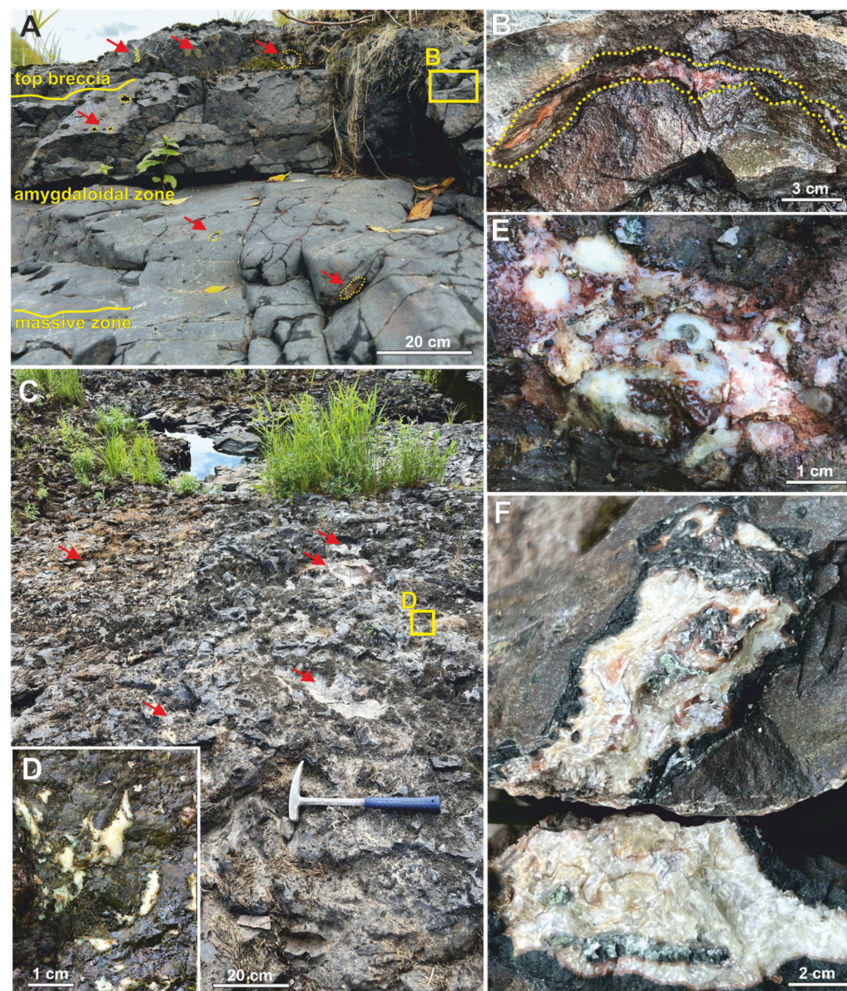


Figure 2. Field outcrop photographs illustrating agates' location in the Mesoproterozoic volcanics within the Pasha–Ladoga Basin (Priozersk Formation). (A) the upper part of lava flow with the massive, amygdaloidal and breccia zones within the coastal cliffs on the Tulemajoki River; (B) vein agate in the inter-breccia lava space, (C) brecciated top of the lava flow; (D) enlarged fragment from selected area of (C) showing agates in the inter-clastic lavas space, (E) cavity infilling with Fe-enriched agate; (F) large gas vesicles within the massive lava filled with agate. Red arrows point to the location of agate mineralization within the lavas.

In the thin lava flows, porphyritic structures are rare; they are characterized by homogeneous massive texture and top lava-breccia. The lavas exhibit a grayish-brown, rarely brownish colour. The tuff material with local gradational bedding is recognized between lava flows. The tuffs are represented by agglomerate and, to a lesser extent, by bomb varieties. The volcanic clasts with the thin chill zones range from 0.2 to 20 cm in size. The matrix is represented by chloritized pelitic material. The fragments of feldspars and granites are occasionally observed within the agglomerate tuffs [10] (pp. 74–75).

The individual zones of vesicular basalts (mandelstones) with the thickness of 5–30 cm are locally recognized within the top massive lava flows. Mineralized vesicles compose up to 80% of the rock volume, their size ranging from 2 to 20 mm (Figure 3). They have usually rounded, elongated shapes or shapes of coalesced amygdaloids, and they are characterized by light-green or red-brownish coloration. The amygdaloids have different orientation, and most of them exhibit concentric zoning.

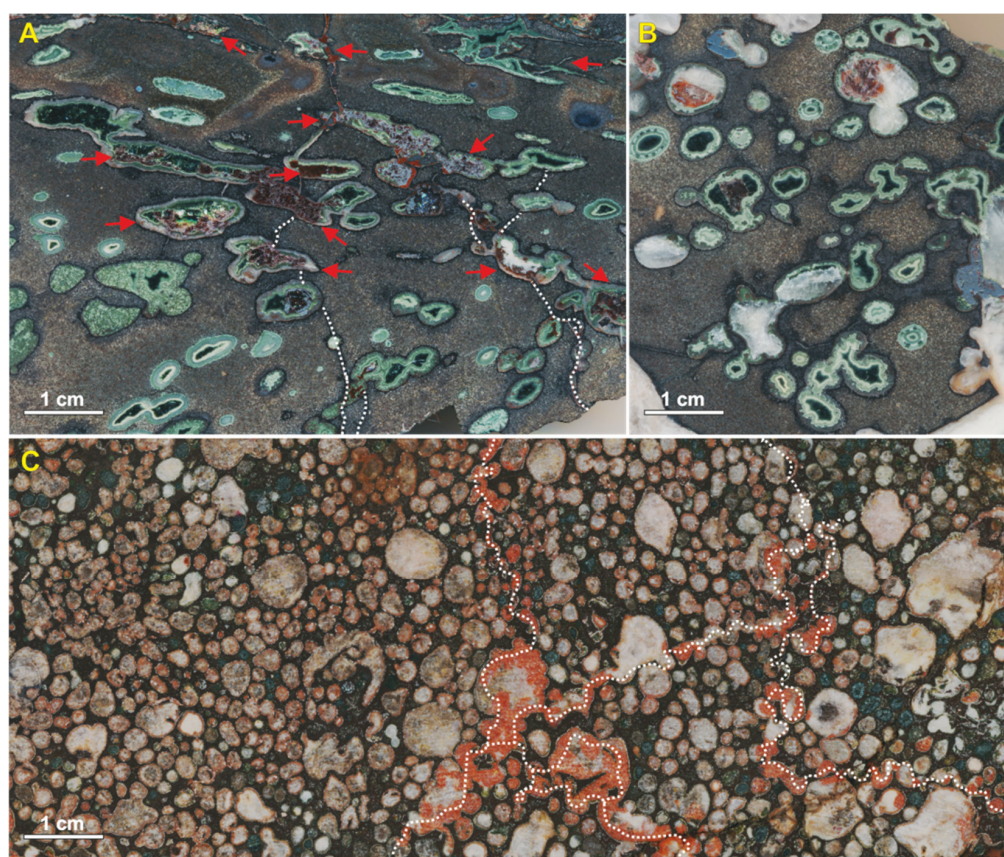


Figure 3. Photographs of the polished slabs of Mesoproterozoic vesicular basalts from the Priozersk Formation within the Pasha–Ladoga Basin. (A,B) Images illustrating concentrically zoned amygdaloids tend to be filled with chlorite. Red arrows point to deformed amygdaloids and fissures with iron oxides appearance. (C) Image showing dense accumulation of rounded and irregularly formed amygdaloids with red-brownish pigments. Dotted lines point to channels of Fe-bearing solution supply.

Agate mineralization is mainly exposed in the upper part of PrF lava flows. Agates are widespread as an infill of fissures, gas vesicles in lavas, and an infill of cavities in slags and lava-breccias (Figure 2B–F). Most agates are round-shaped nodules and veinlets, their size ranges from 1 to 15–20 cm. The frequency of agate occurrence is about of 3–14 per 10 m² of the lava flow surface (Figure 2A,C). According to the data of Polekhovskiy and Punin [9], agates were also found in cores of boreholes drilled in the area of Salmi village. They fill gas vesicles in basalts, cavities in frothy lavas, as well as occur as pebbles in conglomerate and gravelstone beds of the SaIF, overlying the PrF volcanic rocks.

4. Materials and Methods

The Salmi agates and parent volcanic rocks were examined using optical microscopy, scanning electron microscopy with energy-dispersive spectroscopy (SEM-EDS), X-ray fluorescence (XRF), powder X-ray diffraction (XRD), Raman spectroscopy, inductively coupled plasma mass spectrometry (ICP-MS), wet chemistry at the Institute of Geology, Karelian Research Centre, RAS (IG KRC RAS, Petrozavodsk, Russia).

Six agate-bearing volcanic rocks samples (including two samples of vesicular basalts) and two agate nodules with visually different chalcedony/calcite ratio (calcite-rich and calcite-poor samples) were selected from the broad author's collection for detailed mineralogical and geochemical investigation. Additionally, a macrocrystalline quartz sample and three crystalline calcite samples extracted from individual agate nodules were used for geochemical and C-O isotope analysis. Polished thin sections and powders were prepared for the studies.

Standard petrographic investigations were carried out using the Polam-211 optical microscope. The SEM-EDS analyses were applied to determine the chemical composition of the mineral phases comprising the agates. The experiments were performed using a VEGA II LSH (Tescan, Brno, Czech Republic) scanning electron microscope with EDS INCA Energy 350 (Oxford Instruments, Oxford, UK) on carbon-coated, polished thin section. The analyses were carried out at the following parameters: W cathode, 20 kV accelerating voltage, 20 mA beam current, 2 μm beam diameter, and counting time of 90 s. The following standards were used: calcite, albite, MgO, Al₂O₃, SiO₂, FeS₂, wollastonite, Fe, Zn, and InAs. SEM-EDS quantitative data and determination of the analysis accuracy were acquired and processed using the Microanalysis Suite Issue 12, INCA Suite version 4.01.

The concentrations of major elements in the agate-bearing volcanics were determined by wet chemistry and XRF. XRF analysis was performed using an ARL ADVANT'X-2331 (Thermo Fisher Scientific, Ecublens, Switzerland) wavelength-dispersive spectrometer with a rhodium tube, working voltage of 60 kV, working current of 50 mA, and resolution of 0.01. Preliminarily, 2 g of each powdered sample was heated in ceramic crucibles, at 1000 °C, in a muffle furnace for 30 min. The loss of ignition was determined by a change in the mass of the sample after heating. For XRF measurements, 1 g of heated sample was mixed with Li-tetraborate flux and heated in an Au-Pt crucible to 1100 °C to form a fused bead.

The concentrations of trace and rare-earth elements were determined by ICP-MS using an X Series 2 (Thermo Scientific, Bremen, Germany) mass spectrometer. The powdered samples were digested in an acid mixture following the standard procedure [22]. The accuracy of the analyses was monitored by analysing the USGS standard BHVO-2 (see Supplementary Materials, Table S2).

The concentrations of the trace element and rare earth elements were normalized to the concentrations in chondrite (C1) and primitive mantle (PM) [23]. Parameters were calculated: Nb anomaly as $\text{Nb}/\text{Nb}^* = \text{Nb}_n / (\text{Th}_n * \text{La}_n)^{1/2}$, Sr anomaly as $\text{Sr}/\text{Sr}^* = \text{Sr}_n / (\text{Pr}_n * \text{Nd}_n)^{1/2}$ and Eu anomaly as $\text{Eu}/\text{Eu}^* = \text{Eu}_n / (\text{Sm}_n * \text{Gd}_n)^{1/2}$.

Powder XRD analysis was carried out using a Thermo Scientific ARL X'TRA (Thermo Fisher Scientific, Ecublens, Switzerland) diffractometer (CuK α -radiation ($\gamma = 0.1790210$ nm), voltage 40 kV, current 30 mA). Diffractograms of agate samples in the range of 5–75° 2 θ were recorded at a scanning step of 0.40 2 θ /min. X-ray phase analysis was performed using the program packWin XRD, ICCD (DDWiew2008). The detection limit for XRD phase identification was 3 wt%.

Raman spectroscopy was used to identify mineral phases (SiO₂, Fe-oxides, Mn-oxides) in agates. Raman spectroscopy analysis was conducted on a dispersive Nicolet Almega XR Raman spectrometer (Thermo Fisher Scientific, Waltham, MA, USA) with a green laser (532 nm, Nd-YAG (Thermo Fisher Scientific, Waltham, MA, USA)). The spectra were collected at 2 cm⁻¹ spectral resolution. A confocal microscope with a 50 \times objective was used to focus an excitation laser beam on the sample and to collect a Raman signal from a 2 μm diameter area. Raman spectra were acquired in the 85–4000 cm⁻¹ spectral region, with the

exposition time between 30 s and 100 s for each scan, depending on the signal intensity and laser power of 2–10 mW to prevent any sample degradation.

Isotope studies of agate-associated calcite samples were carried out at the Institute of Geology, Komi Scientific Center, Uralian Branch, RAS (IG Komi SC UB RAS, Syktyvkar, Russia). The decomposition of calcite in phosphoric acid and the C-O isotopic composition measurement by flow mass spectrometry (CF-IRMS) were carried out on the Thermo Fisher Scientific analytical complex, which includes a Gas Bench II sample preparation and injection system connected to a mass spectrometer DELTA V Advantage. The $\delta^{13}\text{C}$ values are given in per mille relative to the PDB standard, $\delta^{18}\text{O}$ —the SMOW standard. The international standards NBS 18 and NBS 19 were used for calibration. The analytical precision for $\delta^{13}\text{C}$ and $\delta^{18}\text{O}$ was ± 0.15 ‰ (1σ).

5. Results

5.1. Host Rock Characteristic

The studied volcanics are mostly aphyric and porphyritic with phenocrysts composed of zoning plagioclase crystals with labradorite composition. Plagioclase, augite, and forsterite are the major rock-forming minerals of PrF volcanics. Dominating accessory minerals are apatite, titanite, chlorite, epidote, magnetite, titanomagnetite, ilmenite.

The geochemical differentiation of the PLB volcanic rocks is variable. Using the SiO_2 (49.24–62.01 wt%) and $\text{Na}_2\text{O} + \text{K}_2\text{O}$ (4.42–5.93 wt%) content, volcanic rocks are classified as trachybasalt, basaltic andesites, andesites of the alkaline/subalkaline series (Table 1, Figure 4). Basalts and andesites dominate in the studied succession. In accordance with FeO_{tot} (12.61–15.76 wt%) and TiO_2 (2.13–3.87 wt%) content, volcanics belong to the Fe-Ti-rich type.

Table 1. Chemical composition of agate-bearing volcanics from the PrF, wt %.

Sample	SiO_2	Al_2O_3	Fe_2O_3	FeO	Na_2O	CaO	K_2O	MgO	MnO	TiO_2	P_2O_5	S	LOI	H_2O	Σ
B-1 *	46.6	13.39	9.04	4.6	4.99	3.74	0.59	6.14	0.18	3.64	1.09	0.04	4.74	0.86	99.6
B-2 *	47.5	15.03	11.75	3.45	4.95	3.02	0.74	5.15	0.09	3.54	1.22	0.03	2.72	0.72	99.6
MBG-2 *	58.72	10.72	8.33	4.3	3.86	3.15	0.43	3.86	0.15	2.5	0.92	0.02	2.45	0.55	99.94
MBG-3 *	59.98	9.9	7.6	4.6	4	2.95	0.42	4.29	0.14	2.06	0.75	0.03	2.46	0.4	99.55
MBR-5 **	43.43	5.81		9.42	BDL	17.94	2.01	3.68	0.22	1.58	0.54	-	15.32	-	99.95
MBR-6 **	42.83	6.36		10.21	BDL	16.76	2.51	3.37	0.27	1.81	0.6	-	14.98	-	99.7

Measurements were obtained using wet chemistry (*) and XRF analysis (**). Samples: B-1,2—massive basalts; MBG-2,3—vesicular basalts with light-green amygdaloids; MBR-5,6—vesicular basalts with red-brownish amygdaloids. For (**) samples, FeO values are total FeO. BDL—below XRF detection limit; (-) no data.

The massive lavas are more primitive and differ from vesicular basalts by the lower contents of SiO_2 (<50 wt%), elevated MgO (5.34–6.53 wt%), Al_2O_3 (14.24–15.58 wt%), and P_2O_5 (>1 wt%) contents.

Mandelstones with light-greenish amygdaloids compared to the mandelstones with red-brownish ones are enriched in Al_2O_3 (9.9–10.7 vs. 5.8–6.3 wt%) and Na_2O (3.8–4 wt% vs. below detection limit), but depleted in CaO (~3 wt% vs. ~18 wt%) and MnO (~0.15 wt% vs. ~0.3 wt%). The high content of CaO in mandelstones with red-brownish amygdaloids is probably caused by a local hydrothermal alteration of volcanic rocks. This observation is confirmed by the anomalously high LOI values (up to 15.32 wt%, compared to common values 2.72–4.74 wt%).

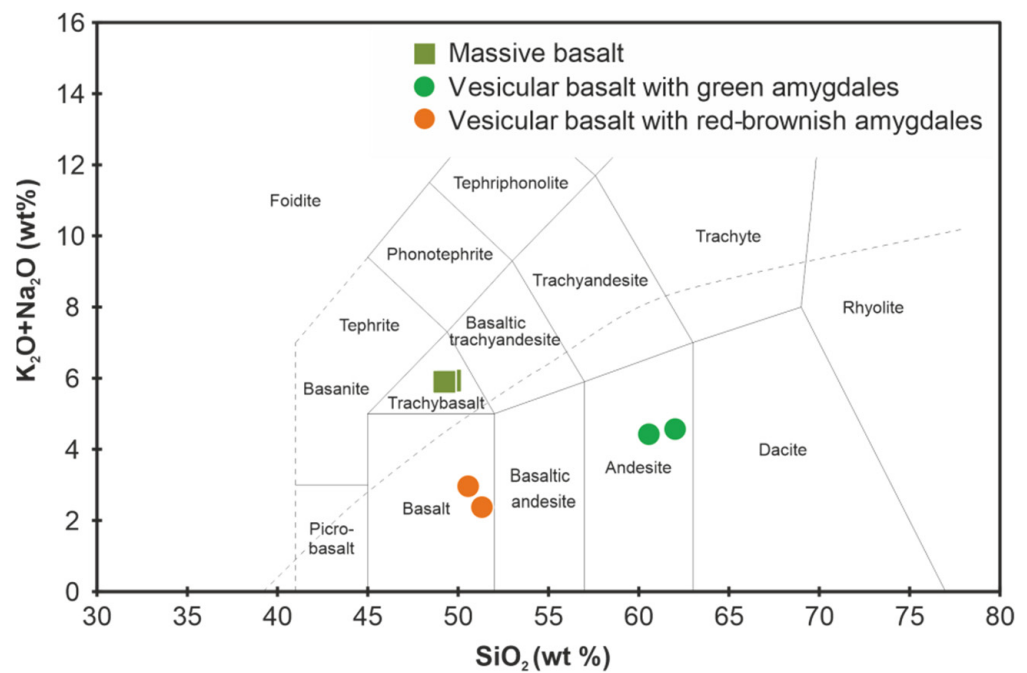


Figure 4. Total alkali silica (TAS) diagram classification (after [24]) of volcanics from the Priozersk Formation within the Pasha–Ladoga Basin.

5.2. Macro- and Microscopic Characteristics of the Agates

The Salmi agates are characterized by specific red-brownish coloration (Figure 5). The colour likely results from chromogenic Fe-oxides compounds disseminated within the agate matrix [25]. The agate nodules often exhibit concentric zoning patterns (Figure 5A,C,E). Some of them are characterized by distinct coarse (1–2 cm) and fine (from few micrometres) banding (Figure 5A), poor-fancy agate varieties are also widespread (Figure 5B,D). Frequently agates contain large calcite and/or quartz crystals. Aggregations of chlorite inclusions were commonly observed in the contact area to the host rock (Figure 5E).

The petrographic study revealed various microtextures of agates. The silica matrix of agates is represented by micro- and macro-crystalline quartz, length-fast chalcedony (with c-axis oriented perpendicular to the fibre direction), as well as zebraic chalcedony (length-fast with a helical twisting of fibres along fibre direction) (Figure 6). These silica phases form banded zones, micro-geodes, and radial fibrous spherulites varying both in thickness and number of concentric layers (Figure 6A,C,E,G). Agates contain an appreciable quantity of calcite phases in the form of elongated or isometric crystals up to 1 cm in size, grained aggregates in the intergrowth with chalcedony, as well as fine-grained aggregates filling the fissures crosscutting the silica matrix (Figure 6C,D). Fine-dispersed Fe-oxide inclusions disseminated along the agate banding emphasize agate zoning (Figure 6B,D,F,H). It is noteworthy that the minute Fe-oxide particles are mostly concentrated within the chalcedony fibres and between microcrystalline quartz grains, whereas macrocrystalline quartz zones are depleted in it.

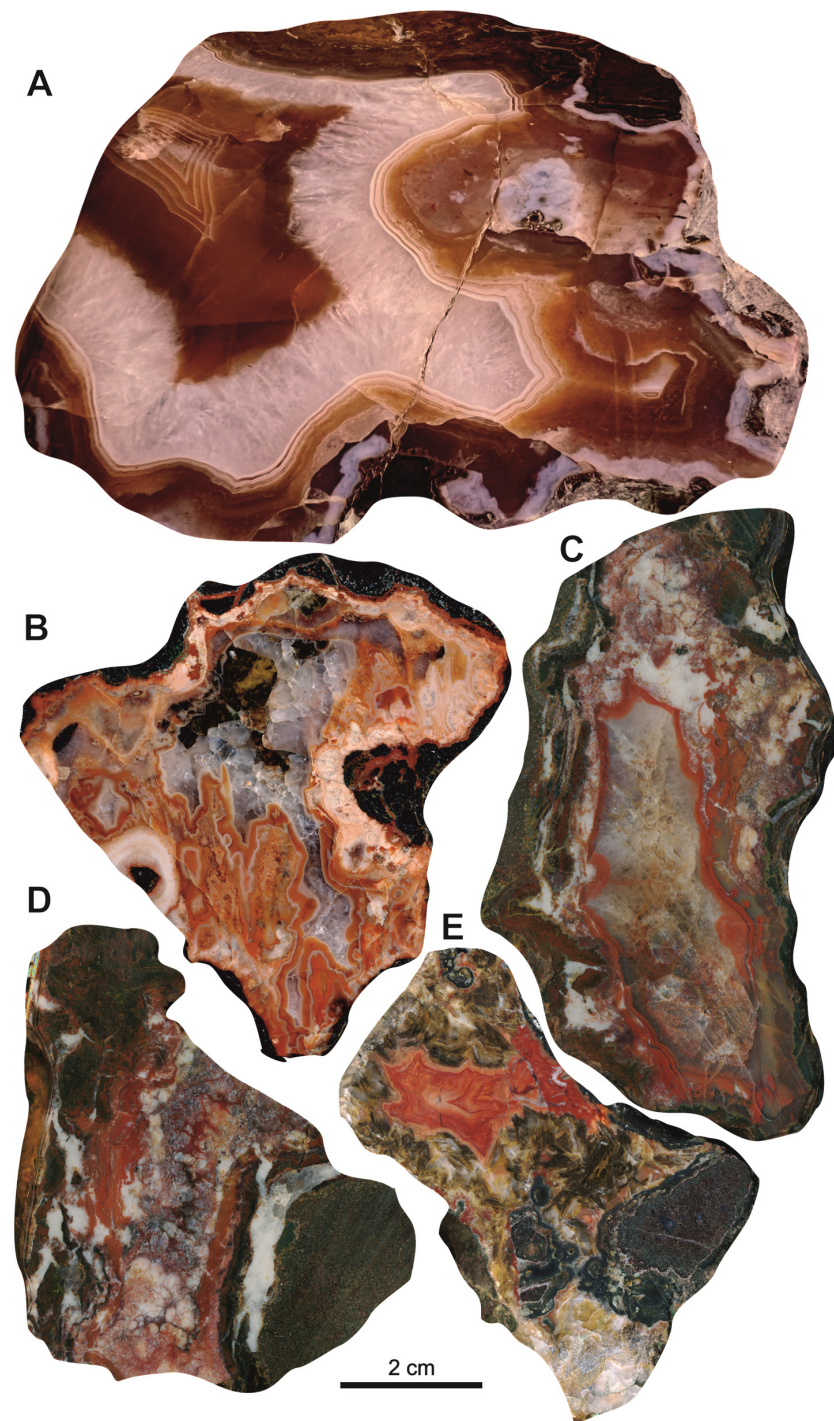


Figure 5. Photographs of agates from the Mesoproterozoic volcanics within the Pasha–Ladoga Basin (Priozersk Formation). (A) Monocentric agate nodule with well-developed concentric zoning and Fe-oxide pigment disseminated along individual chalcedony layers (museum expositional sample of the IG KRC RAS); (B) poor-fancy agate with red-brownish coloured chalcedony and calcite layers, as well as colourless quartz-rich portion; (C) concentrically zoned agate with red-brownish pigment distributed along the external margin of the amygdale; (D) fragment of the vein agate with red-brownish pigment irregularly distributed within chalcedony; (E) concentrically zoned agate surrounded by silica–chlorite matrix.

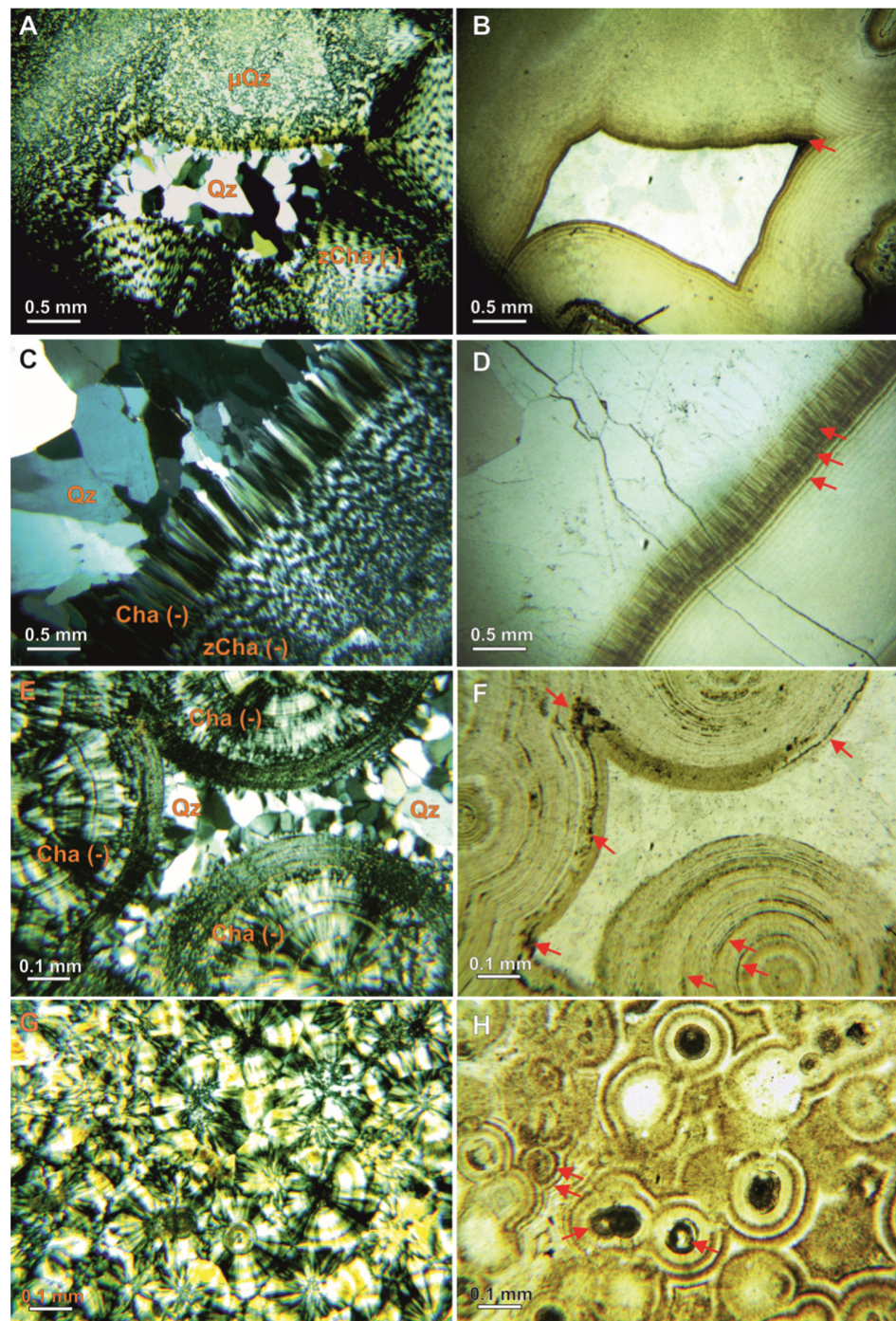


Figure 6. Microphotographs of agates with Fe-oxide pigment: (A,B) microgeode of macrocrystalline quartz within a matrix of microcrystalline quartz and zebraic chalcedony; (C,D) alternate silica phases in the internal part of the agate with microcrystalline quartz, zebraic chalcedony, length-fast chalcedony, macrocrystalline quartz and crosscutting calcite veinlet; (E,F) chalcedony spherulites associated with macrocrystalline quartz; (G,H) dense accumulation of chalcedony spherulites. (A,C,E,G)—polarized light, crossed nicols; (B,D,F,H)—plane polarized light. The micrographs (B,D,F,H) show that the macroscopically visible red colour is caused by the incorporation of Fe-oxide/hydroxide minerals along the chalcedony banding (see arrows). Abbreviations: Cha (-), length-fast chalcedony; zCha (-), zebraic chalcedony; Qz, macrocrystalline quartz; μ Qtz, microcrystalline quartz. The red arrows in figures indicate the location of chromogenic minerals along the strips.

In the studied area, at least two different types of vesicular basalts were distinguished during the macroscopic observation (Figure 3). The first one displays amygdales predominantly light-green in colour due to a high content of chlorite (Figure 3A,B). The amygdales are characterized by elongated, rounded, as well as irregular shapes. It is noteworthy that amygdales with differences in shape and texture can be located directly next to each other (Figure 3A). Additionally, tectonically deformed mineralized vesicles show a significant amount of iron oxides penetrating with the amygdale matrix, whereas intact amygdales are depleted by them (Figure 3A). The other type of vesicular basalts contains amygdales of rounded and, to a lesser extent, irregular forms with close packing (Figure 3C). The larger amygdales tend to be filled with calcite, whereas minute ones can be filled with silica, chlorite, calcite, as well as with their mixture. Most amygdales have a red-brownish tint caused by iron oxides pigmentation. The development of iron oxides is also observed along the fissures connecting the amygdales (Figure 3C).

Microscopic investigation revealed that most of the amygdales exhibiting concentric zoning are composed of successive layers of minute radial fibrous chalcedony, fine-grained, and plate-like chlorite from the margin towards the vesicle centre (Figure 7A–D). Occasionally, amygdales contain macrocrystalline quartz cores (Figure 7E,F). Another zoning type is rarer: amygdales could be filled half with coarse-crystalline calcite and half with concentrically zoned chlorite (Figure 7G). Additionally, gas vesicles could be completely filled with coarse-crystalline calcite or radial fibrous chalcedony (Figure 7H). In the latter case, dusty chlorite is scattered ordinarily between the chalcedony spherulites.

5.3. Mineral Composition

5.3.1. X-ray Powder Diffraction

The X-ray powder diffraction of two bulk agate samples was applied to determine their phase composition. Only peaks corresponding to calcite and alpha-quartz have been identified on the X-ray diffraction patterns (Figure S1). No other silica polymorphs (e.g., opal, cristobalite, tridymite, and moganite) were revealed. The calcite content in one of the examined samples was 69 wt%, while the other sample was poor in calcite.

5.3.2. Raman Spectroscopy Results

Micro-Raman spectroscopy investigation of individual silica bands of agates showed that in all cases, they are only composed of alpha-quartz recognized by the characteristic bands at 464, 353, 208, and 127 cm^{-1} . Numerous Fe-oxide inclusions appeared as needle-like, spherical, irregular grains with a size up to 200 μm distributed in agate nodules and were identified as hematite by their main Raman bands located at 408, 607, 665, 1319 cm^{-1} (Figure 8A,D) [26,27]. The grains of dark minerals surrounding the calcite in agate were evidenced as manganite (MnOOH) according to characteristic Raman bands at 386, 528, 554, 620 cm^{-1} (Figure 8B,E) [28]. Additionally, barite, which frequently occurred in the agates as prismatic crystals with a size up to 0.6 mm surrounded by calcite was identified by its characteristic Raman bands at 453, 461, 617, 647, 988, 1139 cm^{-1} (Figure 8C,F) [29,30].

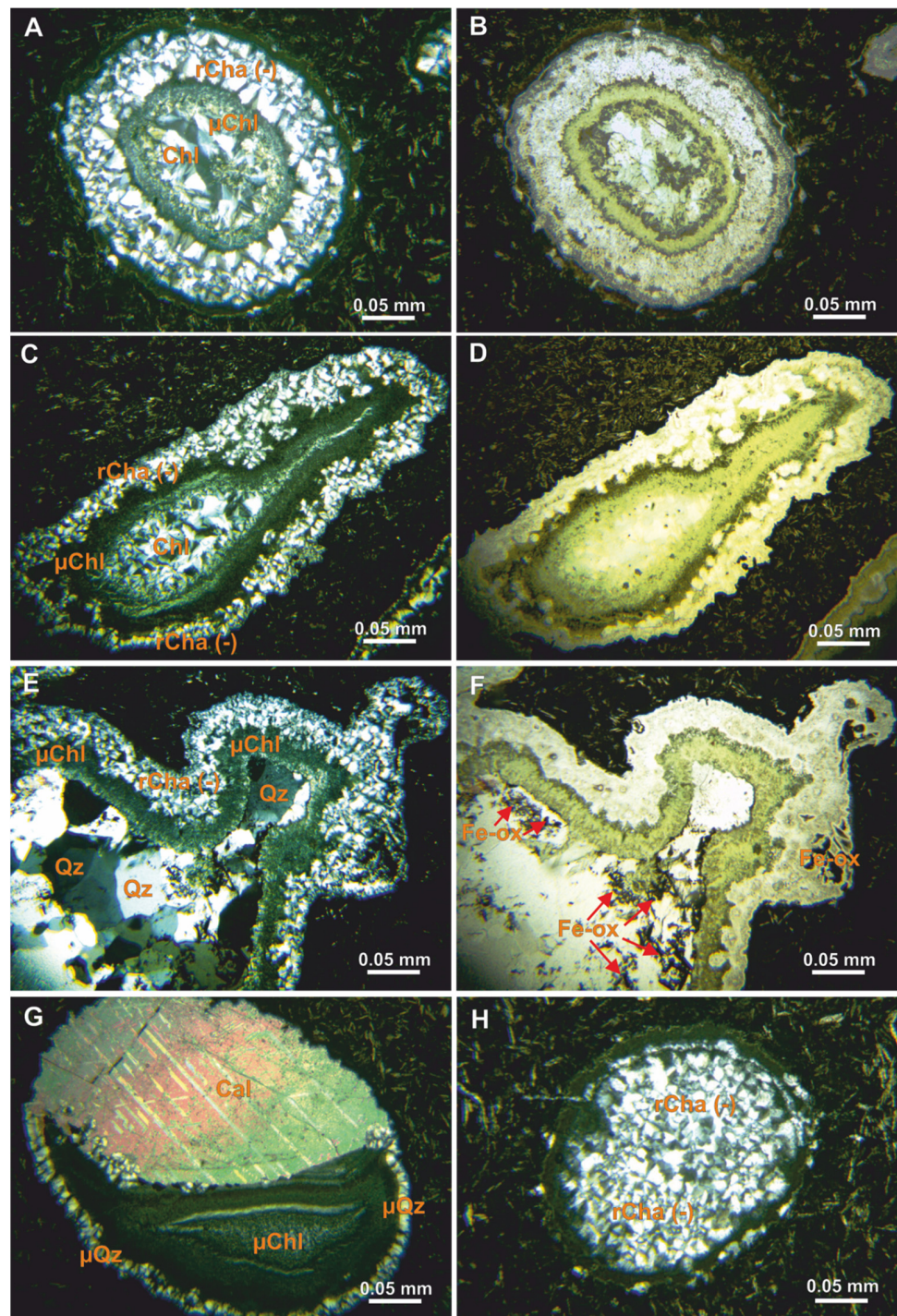


Figure 7. Microphotographs of amygdales in vesicular basalts (mandelstones) from the Priozersk Formation within the Pasha–Ladoga Basin: concentric zoning rounded (A,B) and elongated (C,D) amygdales composed of spherulites of radial fibrous chalcedony, fine-grained and plate-like chlorite; (E,F) irregularly shaped amygdale consisting of radial fibrous chalcedony, fine-grained chlorite, and macrocrystalline quartz core with Fe-oxides in silica matrix; (G) bizoning amygdale composed of calcite and concentric zoning chlorite aggregation; (H) Amygdale uniformly filled with radial fibrous chalcedony. (A,C,E,G,H)—polarized light, crossed nicols; (B,D,F)—plane polarized light. Abbreviations: Cha (-), length-fast chalcedony; rCha (-), radial fibrous chalcedony; Qz, macrocrystalline quartz; μQz, microcrystalline quartz; Chl, plate-like chlorite; μCha, fine-grained chlorite.

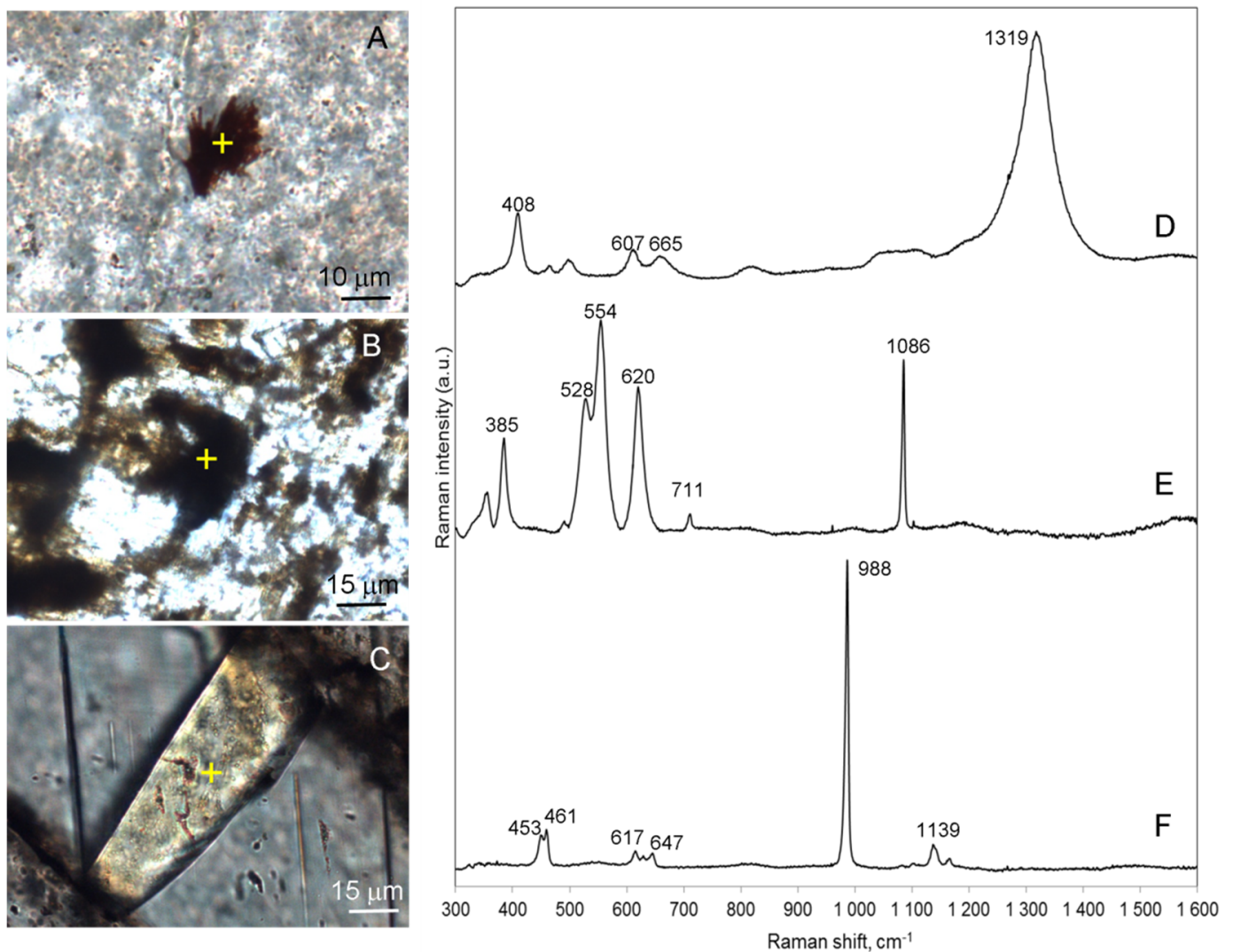


Figure 8. Micrographs (transmitted light mode) and Raman spectra of hematite (A,D), manganese (B,E), and barite (C,F) inclusions in the agates in the spectral range of 300–1600 cm^{-1} . The analytical spots are marked by yellow crosses. Bands at 711, 1086 cm^{-1} on Figure (E) corresponds to calcite.

According to the local Raman study of mineralized gas vesicles in mandelstones, they are filled with alpha-quartz, calcite, and chlorite. The plate-like chlorite crystals predominantly fill the central parts of greenish zoned amygdales from either mandelstone types are characterized by similar Raman bands at 355–367 cm^{-1} , 541–548 cm^{-1} , 673–677 cm^{-1} , and diffused bands at 3600–3657 cm^{-1} (Figure 9). The apparent downshift in the Si-O-Si related Raman band to 673–677 cm^{-1} (from the 681–683 cm^{-1} of Mg-rich chlorite) [31], together with the high intensity of the band at 355–367 cm^{-1} suggest an intermediate Mg-Fe composition of examined chlorites. In the spectral range of $\text{H}_2\text{O}/\text{OH}$ vibrations (3400–3700 cm^{-1}), the Raman spectral patterns from studied chlorite samples show insignificant variations, which are most probably related to different proportions of Mg and Fe in the structure of chlorite [32].

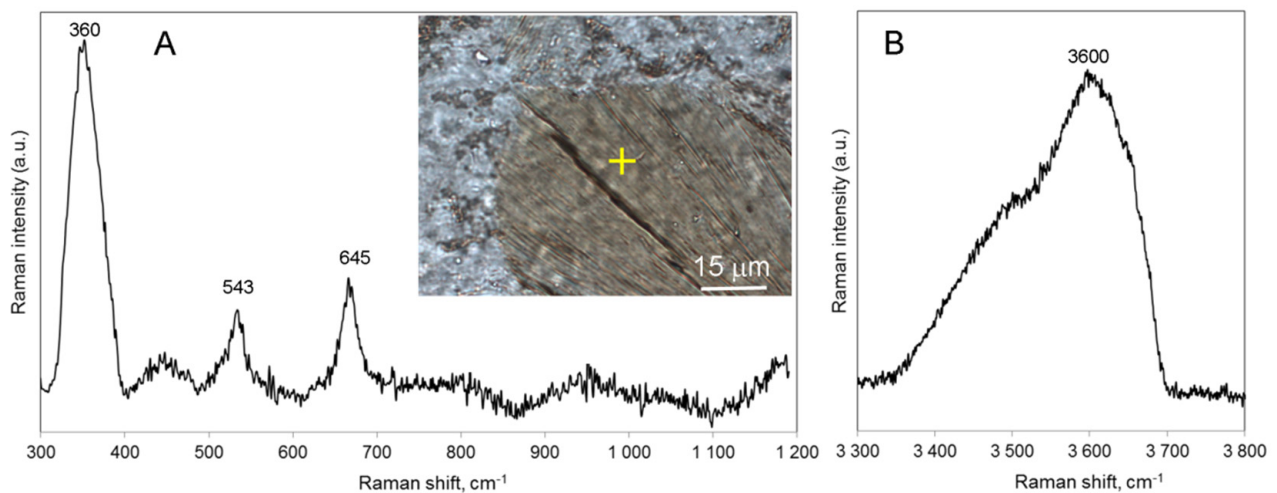


Figure 9. Micrographs and Raman spectra of plate-like chlorite in the amygdale of vesicular basalts in the spectral range of 300–1200 cm^{-1} (A) and 3300–3800 cm^{-1} (B). The analytical spot is marked by a yellow cross.

Red-brownish spherical, needle-like, and crystalline inclusions within the amygdales were all identified as hematite by their characteristic Raman bands. No other Fe-oxide/hydroxide phases were found.

5.4. SEM-EDS Investigation

More evidence concerning the mineral composition of the agates from PLB volcanics was obtained by SEM-EDS investigation. In general, the mineral assemblage of agate nodules and amygdales from vesicular basalts is similar. Banded agate zones are related to the difference in porosity of individual silica layers (Figure 10A). In the higher porosity area scattered needle-like crystals of Fe-oxide and minute inclusions of barite have been concentrated (Figure 10A). Inclusions of Fe-oxide composition often appear at the fissures both in the amygdales and agate nodules (Figure 10B). Fe-oxide phases in the form of large idiomorphic crystals or spherulitic aggregates randomly arranged both in nodules and amygdales are also observed (Figure 10C,D). The most examined Fe-oxide phases are Ti-rich (up to 3 wt%). Numerous barite crystals frequently form clusters embedded within the calcite matrix (Figure 10E). Pseudomorphs of calcite after silica frequently forming banded pattern were revealed in the internal parts of some agates (Figure 10B).

The chemical compositions of chlorites occurring both in agate nodules (Figure 9H) and amygdales of mandelstones (Figure 10D) are characterized by high FeO and MgO contents (Table S1). The total FeO content of chlorite hosted in nodules (21.6%–27.3%) is slightly higher than that in the amygdales (17.0%–23.4%). The MgO content is 12.9%–15.7% and 16.0%–21.6% in chlorite from nodules and amygdales, respectively. It is noteworthy that chlorite compositions of amygdales recorded for both types of mandelstones are generally similar. Alkali contents ($\text{CaO} + \text{K}_2\text{O} + \text{Na}_2\text{O}$) are low and do usually not exceed 1 wt%.

The EDS data from chlorite occurring both in agate nodules and amygdales of mandelstones are used to calculate the structural formulae based on the 20 oxygens (Table S1). The data indicated that chlorite composition is quite homogeneous. In the Al(IV)-Mg-Fe ternary diagram [33], chlorite markers of the amygdales are plotted in the Mg-rich chlorite domain, whereas agate nodules markers are on the limit with Mg-chlorite and Fe-chlorite domains (Figure 11A). The Si vs. $\text{Fe}/(\text{Fe} + \text{Mg})$ classification diagram of Hey [34] displays that examined chlorite samples mainly fall in/near the diabantite field (Figure 11B).

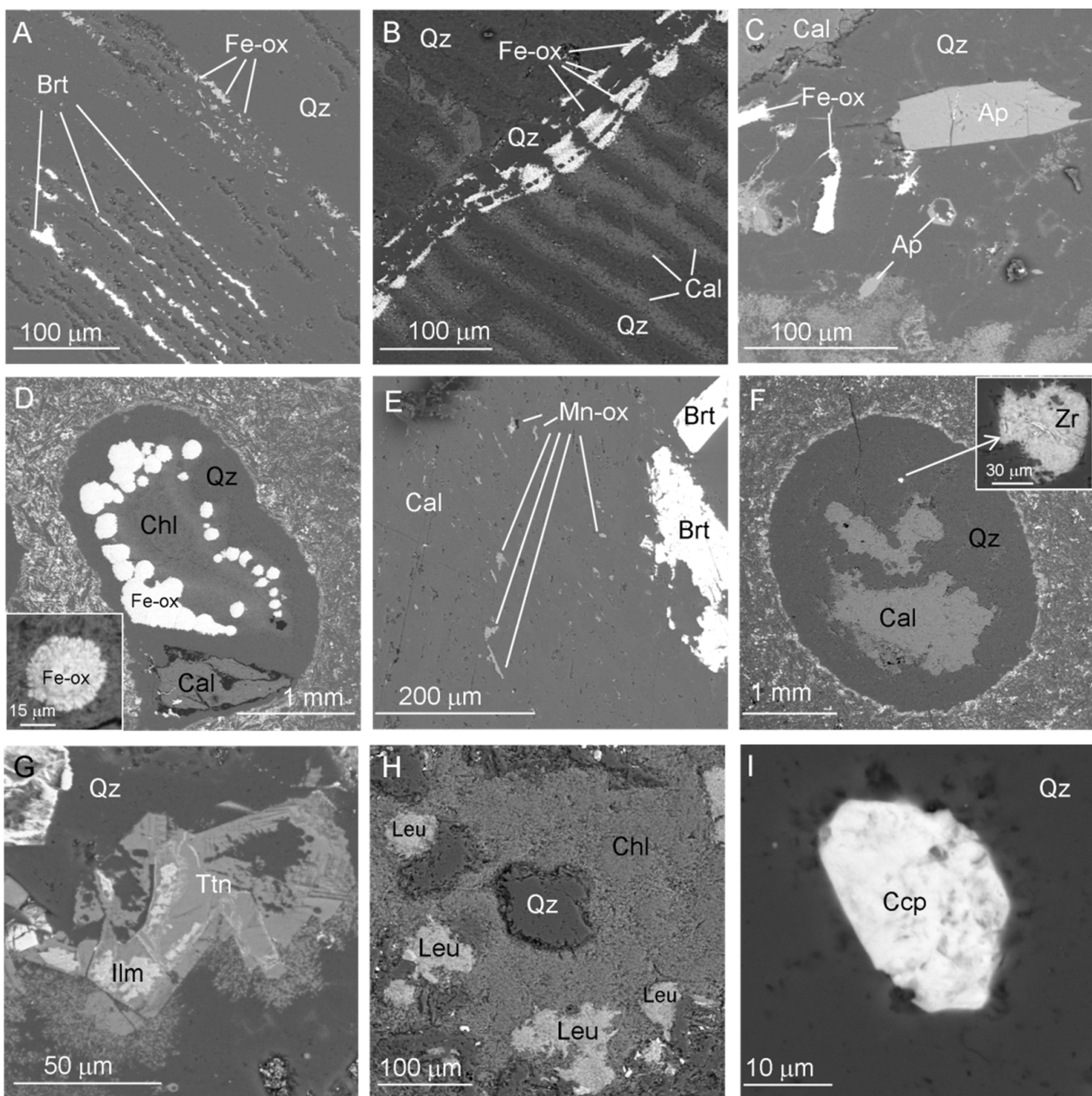


Figure 10. BSE images of microinclusions in agates: (A) Fe-oxides and barite (Brt) scattered along high porosity chalcidony bands in agate nodule; (B) a fissure filling with silica and Fe-oxides, which cross-cuts the banding agate area formed by chalcidony and calcite layers; (C) apatite (Ap) and Fe-oxide inclusions in silica area of agate nodule; (D) spherical aggregates of Fe-oxides arranged in a concentricly zoned amygdale and large calcite (Cal) crystal-filled cavity (enlarged image of spherical inclusion inserted on (C) from the lower left); (E) Mn-oxides and large barite aggregates accompanied by calcite area of agate nodule; (F) corroded grain of zircon (Zr) within the amygdale of quartz-calcite composition; (G) titanite (Ttn) and ilmenite (Ilm) aggregates surrounded by quartz (Qz) in agate nodule; (H) flaky leucoxene (Leu) enclosed by chlorite (Chl) in agate nodule; (I) grain of chalcopyrite (Ccp) in quartz (Qz) matrix within the amygdale of vesicular basalt.

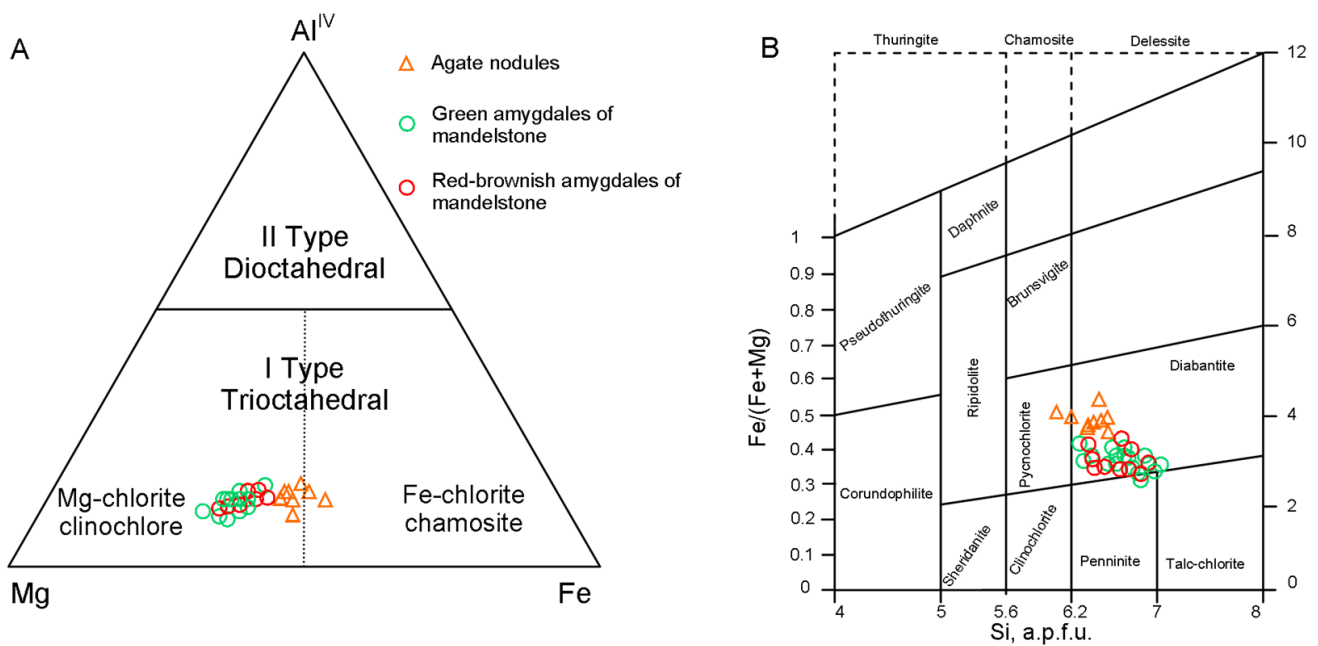


Figure 11. Chlorite classification diagrams showing the position of the investigated samples of the agates. (A) (Al)–Mg–Fe diagram (after [33]); (B) Si vs. Fe/(Fe+Mg) diagram (after [34]).

Additionally, manganese hydroxide, hydroxyapatite, titanite, leucosene, rutile, ilmenite, muscovite were recorded as characteristic mineral inclusions for the Salmi agates, whereas sulphide minerals (pyrite, chalcopyrite) are extremely rare in them (Figure 10E,G,H,I). In a single case, a corroded grain of zircon within the amygdale of quartz-calcite composition was identified (Figure 10F).

5.5. Geochemical and Isotopic Characterization

5.5.1. Trace Elements

ICP-MS trace element analyses of Salmi agates, PrF host volcanics, as well as quartz and calcite separated from agate nodules were carried out to obtain more information about the geochemistry of agates and the mineral-forming fluids (Table S2). Massive and vesicular types of PrF volcanics were all characterized by similar chondrite-normalized rare-earth element (REE) patterns with $\Sigma\text{REE} = 179\text{--}367$ ppm, enrichment in light rare-earth elements (LREE), slight depletion in heavy rare-earth elements (HREE) ($[\text{La}/\text{Sm}]_n = 2.48\text{--}3.19$; $[\text{Gd}/\text{Yb}]_n = 1.62\text{--}2.30$), as well as the minor negative Eu anomaly ($\text{Eu}/\text{Eu}^* = 0.77\text{--}0.95$) (Figure 12). Additionally, volcanic rocks are significantly enriched in Rb, Ba, Zr, Nb and F (0.16%–0.25%) and exhibit a strong negative Sr anomaly ($\text{Sr}/\text{Sr}^* = 0.09\text{--}0.12$) (Figure 13). Elevated concentrations of Rb (37 ppm), Ba (1390 ppm), Mn (2200 ppm), Cs (0.6 ppm) and depleted concentrations of P, Sc, Ti, Cr, Co, Ni, Cu, Ga, Sr, Y, Zr, Nb, Mo, REE in mandelstones with red-brownish amygdals compared to mandelstones with green amygdals were determined.

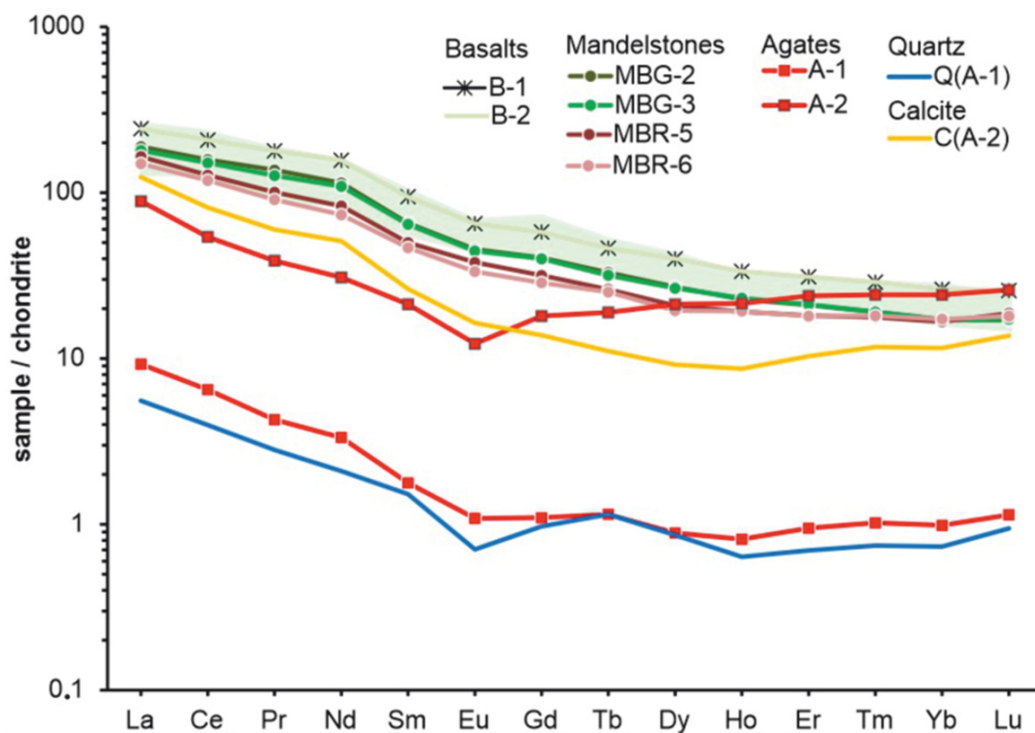


Figure 12. Chondrite-normalized REE distribution patterns for Salmi agates (including quartz and calcite samples extracted from agates) and host volcanic rocks of the Priozersk Formation. The normalization values are from [23]. Green field: the composition of the Late Permian High-Ti continental rift basalts in the Songpan–Ganzi Terrane (South China Block) [35].

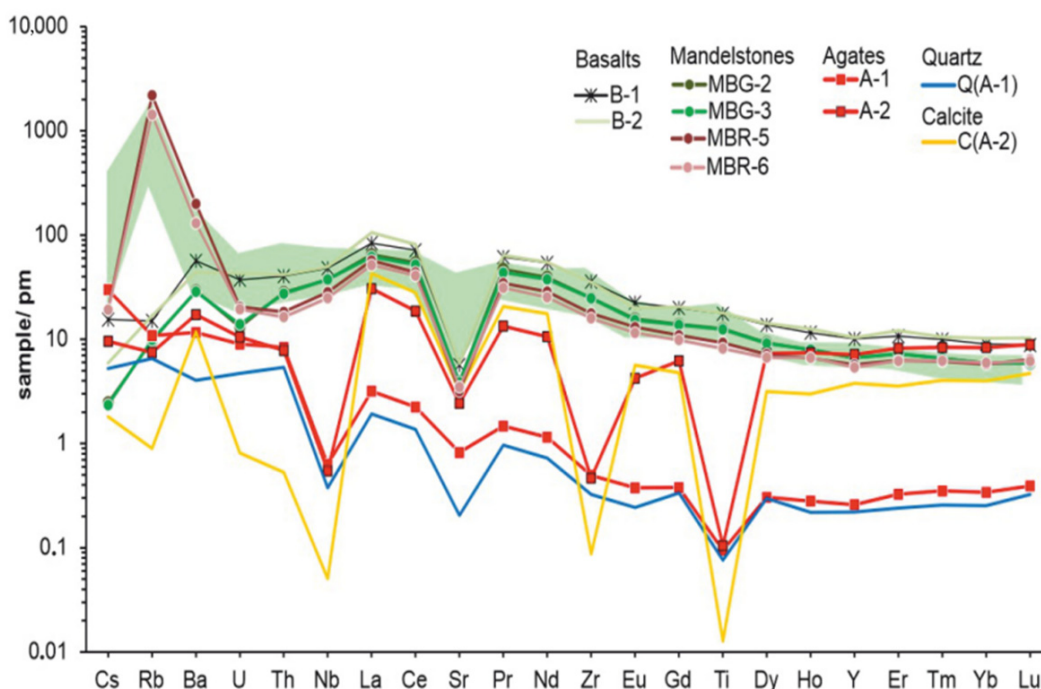


Figure 13. Primitive mantle-normalized trace element distribution patterns for Salmi agates (including quartz and calcite samples extracted from agates) and host volcanic rocks of the PLB. The normalization values are from [23]. Green field: the composition of the Late Permian High-Ti continental rift basalts in the Songpan–Ganzi Terrane (South China Block) [35].

The concentration of the most trace elements in agates is much lower than in the host volcanic rocks (Table S2). Two examined agate nodules with various quartz/calcite ratio exhibit REE distribution trends with enrichment of LREE ($[La/Sm]_n = 4.04\text{--}5.07$), and slightly negative Eu anomaly ($Eu/Eu^* = 0.62\text{--}0.78$) (Figure 12). However, they are characterized by difference in distribution of HREE and different levels of REE content. The calcite-rich agate has slightly enrichment of HREE, while calcite-poor agate is characterized by unfractionated HREE trend. The ΣREE are 9 and 97 ppm for calcite-poor (A-1) and calcite-rich (A-2) samples, respectively. The pattern of the REE distribution for the studied agates slightly differs from that for the host rocks. The degree of LREE enrichment of agates ($[La/Sm]_n = 4\text{--}5$) is higher than that of volcanics ($[La/Sm]_n = 2\text{--}3$), but the degree of HREE enrichment ($[Gd/Yb]_n = 0.7\text{--}1$) in agates is lower than that for volcanics ($[Gd/Yb]_n = 1.9\text{--}2.3$). Salmi agates have very low V, Cr, Co, Ni, Cu, Zn, Ga, Sr, Zr, Nb, Mo, Cd, Sn, Ba, Hf, Ta, W, Pb, Th concentrations. In contrast, elements such as Mn (max 5302), Ti (max 136 ppm), Li (max 66 ppm), Cs (max 0.96 ppm), and Tl (max 0.78 ppm) are concentrated in them. Only the contents of Rb (4–6 ppm), Sb (0.04–0.07 ppm), and Bi (0.02 ppm) are the same in agates and host rocks.

Microcrystalline quartz hosted in the agate is depleted in the most trace elements compared to the host agate, with the exception of Cr, Cu, Zn, Rb, Sn, Sb, Hf, Ta, Tl and Bi (Figure 13, Table S2). The quartz had a lower REE concentration ($\Sigma REE = 6$ ppm) compared with the agates and shows the distinct Eu anomaly ($Eu/Eu^* = 0.58\text{--}0.6$) (Figure 12). The REE distribution pattern of quartz with enrichment in LREE is generally similar to the REE pattern for calcite-poor agate (A-1). In contrast, the agate-associated calcite had a higher total REE content ($\Sigma REE = 124$) than agates and is characterized by a high concentration of Mn (3680 ppm), Ba (83 ppm), Sr (67 ppm), La (29 ppm), Ce (49 ppm), Nd (23 ppm), Y (17 ppm), Ti (16 ppm), Zn (14 ppm), P (11 ppm). The concentration of follow elements are lower: Li, Ni, Cu, Pr, Sm, Gd, Dy, Er, Yb (1–8 ppm); V, Cr, Co, Rb, Zr, Sn, Eu, Tb, Ho, Tm, Lu, Tl, Pb (0.3–0.9 ppm). Content of some trace elements are below the detection limit (0.3 ppm) of the ICP-MS method.

5.5.2. C-O Isotopic Composition

To specify the origin of carbonate material in Salmi agates, the stable isotope composition of agate-associated calcite samples was studied (Table 2). The results show that calcites have narrow $\delta^{13}C$ (-3.4‰ to -6.94‰ , PDB) and $\delta^{18}O$ (24.83‰ to 25.16‰, SMOW) intervals. The correlation diagram $\delta^{13}C/\delta^{18}O$ (Figure 14) displays that the $\delta^{13}C$ values fall within the interval (-2‰ to -8‰) that is typical of mantle carbonate [36]. However, the $\delta^{18}O$ values of examined calcites are significantly higher than those ones that characterize the deep carbon sources and coincide with the values (20‰ to 26‰) that are typical of sedimentary carbonates (normal marine limestone) [37].

Table 2. Carbon and oxygen isotope composition of calcite samples from Salmi agates.

Sample	$\delta^{13}C$ PDB(‰)	$\delta^{18}O$ SMOW(‰)
C-1	−6.94	24.35
C-2	−5.22	25.16
C-3	−3.46	24.83

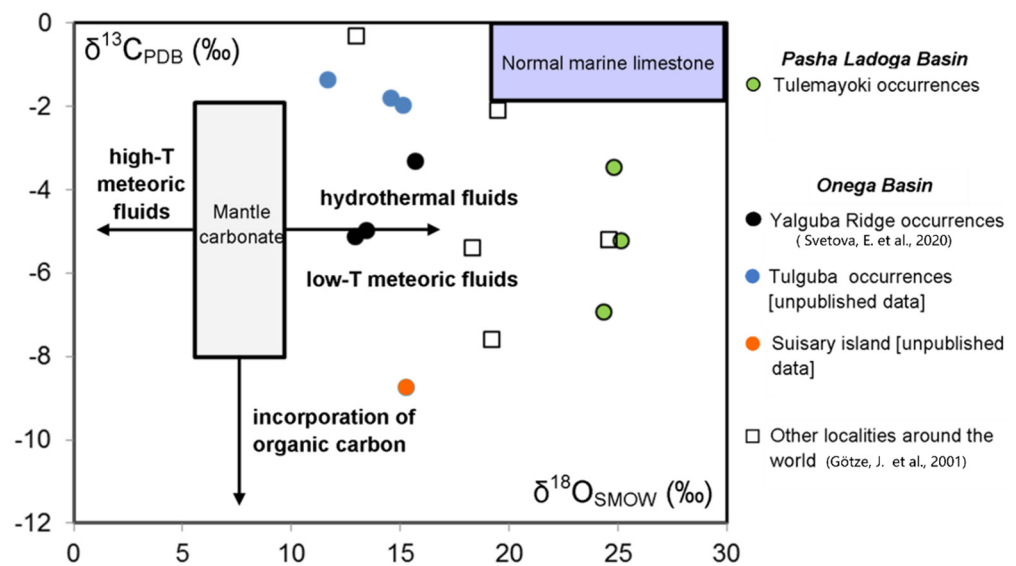


Figure 14. Plot of the oxygen-versus-carbon isotope results for agate-associated calcite samples from the Salmi occurrence (Pasha–Ladoga Basin) along with data available for agates of the Paleoproterozoic Onega Basin (NW Russia) and other localities around the world [3,7]. Mantle carbonate box and trends showing how various processes would affect the C–O isotope composition of magmatic carbonates are given according to Giuliani et al. [36], normal marine limestone [37].

6. Discussion

The obtained data by the integrated mineralogical, geochemical, and C–O isotope investigation of the Salmi agates together with the analysis of published geological materials for the studied area allow the discussion of the agate’s peculiarities in more detail, speculating about coloration origin, agate provenance, and age.

6.1. Agate-Bearing Volcanic Rocks in the PLB

Mesoproterozoic volcanic rocks of the Priozersk Formation within the PLB are the youngest known agate-bearing volcanics at the Southeast Fennoscandia. Agates are mostly associated with massive varieties of basalt, andesites, as well as lava breccias and frothy lavas.

Volcanic host rocks are significantly enriched in Rb, Ba, Zr, and F, characterized by highly fractionated LREE/HREE chondrite-normalized patterns with no significant negative Eu anomaly. The chondrite-normalized REE diagram (Figure 12) exhibits patterns very similar to intracontinental rift basalts (CRB), such as Late Permian High-Ti Basalts in the Songpan–Ganzi Terrane, which mark the continental breakup of the South China Block [34] and close to Eocene–Oligocene alkaline rocks of Tibetan magmatic complex [38].

The low contents of Cr (54–61 ppm) and Ni (25–28 ppm) together with the strong negative Sr anomaly in PrF basalts (Figure 13) indicates crystallization from previously differentiated melts, which were formed at low-degree melting of a metasomatized mantle source containing amphibole and phlogopite [11] (pp. 145–147). Most likely, the primary melts were contaminated with crustal components [11] (pp.146), [19].

The comagmatic intrusive complex for PLB volcanics is the Valaam sill [11] (pp. 145–147), [17,18,21]. It forms a flat intrusive body extending over 2000 km² and exposed on the pre-Quaternary surface of the Valaam archipelago in the northern part of the Ladoga Lake. The Valaam sill intrudes the PrF, SalF, and PashF and is represented by subalkaline ferro-gabbro-dolerites, while more felsic rocks occur in the uppermost part of the intrusion. The U–Pb age of the intrusion is 1457 ± 3 Ma [21].

The geochemical composition of the PLB volcanics and Valaam sill rocks [11] (pp. 145–147) gives evidence of the intraplate character of magmatism (continental rifting), which took place within the Pasha–Ladoga Basin (ca. 1485–1454 Ma).

The obtained data suggest that the agates formation in the Pasha–Ladoga Basin are connected with post-magmatic processes, as well as hydrothermal fluids related to the intrusion of gabbro-dolerite sills (1459–1457 Ma).

6.2. Distribution and Morphology of Salmi Agates

Agates have been recognized in the upper part of PrF within the PLB and also observed as pebbles in conglomerate and gravelstone beds of the SalF [9], overlying the PrF volcanic rocks. Agate mineralization appears mostly as an infill of fissures, cavities, gas vesicles in massive and vesicular basalts, and lava-breccias. The agates are characterized by diverse textures and frequently exhibited concentric zoning patterns. The vein agates most often have a poor-fancy texture pattern (Figure 5D). According to Polekhovskiy and Punin [9], this is determined by the quiet regime of silica deposition from the post-magmatic fluids in a connected system of open cavities. It is assumed that after filling with chalcedony and blockage of silica supply channels, a cavity passes to feeding by diffusion through the micropores of cavity walls and previously precipitated layers [24]. The diffusion of silica and its precipitation lead to oscillatory zoning. The zoning patterns in the individual cavities are varied probably because of variable permeability and rate of silica transfer (Figure 5). As for mandelstones, the vesicles were initially closed, and therefore, an individual regime of silica precipitation is established in each of them. This probably leads to a difference in the microtexture of the closely located amygdales (Figure 3). Additionally, the sporadic presence of discordant-filling vesicles (Figure 7G) indicates that the orientation of the amygdales has been changed during the agates formation under the influence of local tectonics. The abundance of fissures filled with silica, calcite and Fe-oxides in both agate nodules and mandelstones indicates that basalts were subjected to tectonic destructions and at least two phases of agate formation took place.

6.3. Mineralogy and Geochemistry of Salmi Agates

The agates exhibit diversified internal microtextures due to the individual layers composed of micro- and macro-crystalline quartz, length-fast chalcedony, and zebraic chalcedony. An insignificant moganite impurity in Salmi agates was reported by Polekhovskiy and Punin according to X-ray diffraction data [9]. In the present study, X-ray diffraction analysis revealed only alpha-quartz and calcite phases in Salmi agates. No other silica phases beside alpha-quartz in the agates were also identified by the local Raman spectroscopy method. The absence of amorphous silica or other silica phases that appear during its crystallization (cristobalite, tridymite, moganite) is common for agates from relatively old volcanic host rocks that have been subjected to thermal effect [39]. Such silica phases are metastable and thus tend to transform into water-poor α -quartz.

The agates with the characteristic red coloration are widely distributed and have been described for many localities of Germany, Poland, Morocco, China, USA, Russia, etc. (e.g., [4,40–45]). It is shown that such coloration is associated with different types of iron compounds disseminated within the agate matrix.

Petrographic and Raman spectroscopy investigations revealed that the specific red-brownish colour of the Salmi agates (including amygdales in vesicular basalts) is caused by hematite inclusions. These inclusions occur in two main generations. The first one is represented by minute hematite particles (fine-grained or needle-like) aligned along the micro-banding of agate (Figure 6B,D,F,H). Most likely, Fe-oxides and silica precipitated simultaneously from the same primary mineralizing fluids enriched in Fe. The observed agate's banding can be the result of a process of "self-purification" of silica during crystallization [44]. The second one is characterized by large spherical and irregular aggregates randomly distributed within the agate matrix (Figure 7E) or associated with fissures (e.g., Figures 3A and 10B) in which late silica fluids were transported. The abundance of two generations of hematite point to a high activity of iron both in primary silica-bearing fluids and in late hydrothermal solutions. We suggest that late hydrothermal fluids could mobilize the Fe-compounds from the crust of weathering underlying PrF volcanics, which

are then accumulated in vesicles and fissures. As a result, an additional red coloration of the agates appears and hematized zones were formed in the mandelstones.

Besides the abundance of hematite in agates, elevated FeO content in chlorite also indicates a high activity of iron in the agate-forming fluid. The empirical geothermometers based on chemical composition of chlorites are widely used in different geological environments [46–48]. Since examined chlorites can be assigned to Mg-Fe variety and classified as diabantite, we applied a thermometer proposed by Kranidiotis and MacLean [47] to evaluate the chlorite formation temperatures (Table S1). This thermometer is based on the linear relation between Al(IV) in chlorite (with correction using Fe and Mg contents) and temperature. The calculation formula is $T (^{\circ}\text{C}) = 106 (\text{Al(IV)corr}) + 18$, where $\text{Al(IV)corr} = \text{Al(IV)} + 0.7 (\text{Fe}/[\text{Fe} + \text{Mg}])$. As a result, it was found that crystallization temperatures of chlorite from green amygdales (146–232 °C, mean = 189 °C) are slightly lower than those of chlorite from red-brownish amygdales (160–219 °C, mean = 191 °C). Meanwhile, the calculated results of chlorite from agate nodules (206–261 °C, mean = 225 °C) are unequivocally higher than those for amygdales from mandelstones. The estimated chlorite formation temperatures correspond to low-temperature hydrothermal environments. The difference in chlorite formation temperatures between agate nodules and amygdales from mandelstone is probably due to two-stage hydrothermal activities. Crystallization of chlorite apparently occurred under decrease in temperature, first in agate nodules and then in amygdales of mandelstone.

Thus, the mineral assemblage characterising the Salmi agates is predominantly represented by alpha-quartz, calcite, hematite, and chlorite, but it also contains inclusions of barite, hydroxyapatite, titanite, leucosene, rutile, ilmenite, manganite, muscovite, as well as in rare cases, zircon, pyrite, and chalcopyrite. They were probably formed during the post-magmatic processes and/or at the hydrothermal stage.

The comparison of trace element data of agates and agate-bearing volcanic rocks are of special interest in view of the reconstruction of the hydrothermal mineral-forming process [3,49–51]. According to ICP-MS measurements, the agates are depleted in most trace elements compared to host volcanics, which is consistent with data of other investigations [3]. The general REE trends of agates and host volcanics display similarities in enrichment of LREE in regard to HREE and presence of negative Eu-anomaly, which may indicate the mobilization of some elements by circulating post-magmatic fluids from volcanic rocks. However, different fractionation trends for HREE in agate and host volcanics probably point to unrelated sources of their transporting. The common feature is also the absence of a Ce anomaly. The development of positive Ce-anomalies is associated usually with hydrothermal alteration of volcanic rocks [52]. According to petrographic and geochemical data the studied rocks were not subjected to regional alteration.

Elevated (5320 ppm) Mn concentrations (exceeding the values reported for host volcanic rocks) in calcite-rich agate possibly arise from both manganite microinclusions and structural incorporation of Mn within calcite. The quite high Ba (up to 121 ppm) and Ti (to 136 ppm) contents in agates are probably related to barite and titanite inclusions, respectively. Meanwhile, the unexpected high Ti concentrations in quartz sample (98 ppm) may provide evidence for the high temperature of agate crystallization (>200 °C) [53], which has been also suggested on the basis of chlorite data.

The general similarity between REE distribution trends and elevated total REE contents in calcite-rich agates and extracted calcite suggest that calcite is a concentrator of REE. In contrast, the quartz together with calcite-poor agate is characterized by low REE content, which has also been reported in other studies [3,54]. Interestingly, macrocrystalline quartz from the central part of the agate nodule (which was formed on the final stage of agate crystallization) is significantly depleted in trace elements compared to host agate. The decreasing trend of trace element concentration in the banded agates from the outer zone to the core provide by local LA-ICP-MS analyses indicated the chemical purification process during crystallization [2,7,50].

The $\delta^{13}\text{C}$ and $\delta^{18}\text{O}$ values obtained for agate-associated calcite point to unrelated origin of carbon and oxygen (Figure 14). The $\delta^{13}\text{C}$ values in the range ($-2 \dots -8\%$, PDB) probably reflect primary magmatic origin, whereas relatively high $\delta^{18}\text{O}$ values ($24 \dots 25\%$, SMOW) point to a sedimentary source. The close $\delta^{13}\text{C}/\delta^{18}\text{O}$ ratios display agate-associated calcite samples from Phanerozoic and Precambrian volcanics of some other regions in the world (Figure 14). The majority of $\delta^{13}\text{C}/\delta^{18}\text{O}$ markers are in the transition zone between sedimentary carbonates (normal marine limestone) and magmatic carbonates with the influence of hydrothermal or low-thermal meteoric fluids. It is suggested that isotope feature of calcite can be connected with the processes of fluid mixing during formation, where carbon inherits its primary magmatic signature (volcanic H_2CO_3 as the dominant carbon species), whereas the signature of oxygen isotopes is overprinted by the secondary influence of meteoric water [2]. The close C-O isotopic characterization of agate calcite from different localities suggests that agates in volcanic rocks were formed with the active participation of post-magmatic hydrothermal fluids.

6.4. Origin of Agates

Summarizing the data on the mineralogy and geochemistry of Salmi agates from the PrF volcanics obtained in the present study and compilation of a regional geological information [10] (pp. 74–75), [11] (pp.145–147), [12], [17] (pp. 49–50) the agate mineralisation in PLB can be generalized into three stages, as illustrated in Figure 15.

Stage I involves the initial formation of PLB, including accumulation of terrigenous sedimentary rocks of PrF (after ca. 1477 Ma) and appearance of riftogenic volcanics (Figure 15A). The primary agate mineralization occurred after the formation of volcanic rocks of PrF (1485–1460 Ma) (Figure 15B). The upper lava flows were eroded simultaneously with the accumulation of terrigenous sediments of SalF, which resulted in the ingress of agate-bearing basalt fragments into the conglomerate sequence at the SalmF basement (Figure 15C). The migration of post-magmatic fluids toward sediments of SalF was blocked because of low permeability of argillaceous sandstone of SalF.

Stage II involves the formation of volcanic-sedimentary complexes of SalmF and PashF (ca. 1460 Ma) (Figure 15D). The multiphase intrusion of gabbro-dolerite Vallaam sill at 1459–1454 Ma (Figure 15E) most likely results in the formation of tectonically permeable zones at the basement of PLB rocks (Figure 15F). Fluid flows associated with late post-magmatic phases of sill were interacted with basin fluids and remobilized the iron compounds from the crust of weathering.

Stage III (1450–1400 Ma) involves the top-up of previously formed agate nodules and mineralized vesicles by hematite-rich calcite/silica matter, as well as mineralization of newly formed fissures and cavities, including gas vesicles in mandelstones (Figure 15G).

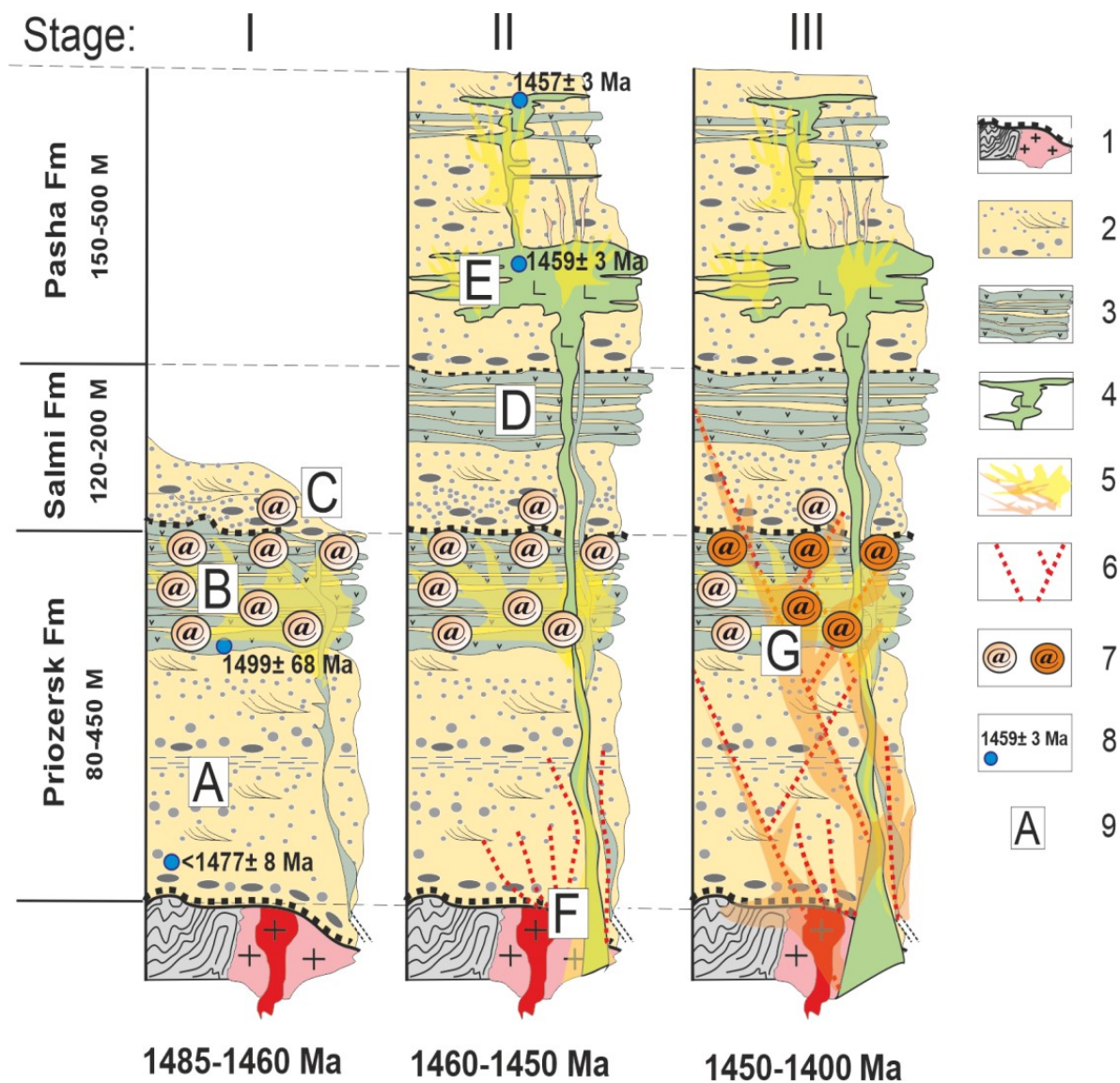


Figure 15. Schematic model of the agate formation stages in the Pasha–Ladoga Basin. Compiled using data from [10] (pp. 74–75), [11] (pp. 145–147), [12], [17] (pp. 49–50). Legend: 1, basement rocks; 2, sedimentary successions; 3, volcanic rocks; 4, Valaam sill; 5, post-magmatic and hydrothermal fluids affected zones; 6, tectonic faults, channels of fluid migration; 7, agates; 8, isotope ages; 9, events associated with the agates formation. The black dotted lines indicate profiles of crust of weathering (erosion rocks areas). Stage I: formation of PLB, accumulation of sedimentary rocks of PrF, and appearance of riftogenic volcanics (A); agate formation within PrF volcanics (B); erosion of upper lava flows of PrF and accumulation of sediments of Salmi (C). Stage II: formation of volcanic-sedimentary complexes of Salmi and PashF (D); intrusion of gabbro-dolerite sill (E); formation of tectonically permeable zones at the PLB basement and remobilization of iron compounds from the crust of weathering (F). Stage III: top-up of previously formed agates and mineralization of gas vesicles by hematite-rich calcite/silica matter (G).

7. Conclusions

The present contribution provides an integrated mineralogical and geochemical investigation of agate gemstones occurring in the Mesoproterozoic volcanic rocks of the PrF (ca. 1485–1460 Ma) within the Pasha–Ladoga Basin (Fennoscandian Shield, NW Russia).

The mineral composition of agates is dominated by alpha-quartz (fibrous chalcedony, microcrystalline and macrocrystalline quartz), but also displays abundances of calcite. The

characteristic red-brownish agate's coloration is caused by multiple hematite inclusion distributed in an agate matrix.

The C–O isotope characteristic of agate-associated calcite points to the processes of fluid mixing during formation, where carbon inherits its primary magmatic origin, whereas the oxygen isotopes are reflected by the secondary influence of hydrothermal or meteoric waters.

The study revealed the two phases of agate formation in the PrF volcanics, which are most likely controlled by two distinctly different fluids and/or their mixture. At first, agates of quartz–calcite–chlorite composition with disseminated minute hematite inclusions appeared due to post-magmatic iron rich fluids. The late hydrothermal activity was probably triggered by the intrusion of the gabbro–dolerite Valaam sill and results in the second phase of agate formation. The hydrothermal fluids remobilized the iron oxides from the crust of weathering underlying the basement of PrF volcanics, which led to formation of vein agate, and filling of gas vesicles with hematite-rich calcite/silica matter. Fluid migration in the PLB was hindered by low permeability of argillaceous sandstone of SaF. Therefore, agates occur only locally in the PrF volcanics within the PLB sequence.

The studied agate occurrence could potentially be the source of a decorative agate gemstones, which is evidenced by single spectacular agate findings. This area is a tourist attraction, but the limited outcrop of the complex does not allow agates to be mined in large volumes.

Supplementary Materials: The following supporting information can be downloaded at: <https://www.mdpi.com/article/10.3390/min13010062/s1>, Table S1: Chemical composition of chlorite from the agate nodules and the amygdales of mandelstones from the PrF of the PLB (EDS microanalysis, wt%); Table S2: Trace elements composition of agate-bearing volcanics and agates from the PrF of the PLB (ppm) and ICP-MS BHVO2 standard results (ppm); Figure S1: X-ray diffractograms of the calcite-poor (A-1) and calcite-rich (A-2) agate samples.

Author Contributions: Conceptualisation, E.N.S. and S.A.S.; investigation, E.N.S. and S.A.S.; data curation, E.N.S. and S.A.S.; writing—original draft, E.N.S. and S.A.S.; visualization, E.N.S. and S.A.S.; compilation of geological published data, S.A.S. All authors have read and agreed to the published version of the manuscript.

Funding: This research was funded by state assignment to the Institute of Geology Karelian Research Centre RAS.

Data Availability Statement: All data are contained within the article and supplementary materials.

Acknowledgments: We are grateful to S.V. Burdyukh, I.S. Inina, and A.S. Paramonov (IG KRC RAS, Petrozavodsk, Russia) and to I.V. Smoleva and V.L. Andreichev (IG Komi SC, UB, RAS, Syktyvkar, Russia) for their assistance in analytical investigations. The authors thank V.I. Ivashchenko (IG KRC RAS, Petrozavodsk, Russia) for donating two agate specimens and the useful advice. We are grateful to O.B. Lavrov (IG KRC RAS, Petrozavodsk, Russia) for consultancy in the field research process. We are thankful to V.I. Ivashenko, A.A. Konyshov and Yu.N. Smirnov for assistance in field investigation in 2022. We also thank three anonymous reviewers and the Academic Editor for their constructive comments, which helped us to improve the manuscript.

Conflicts of Interest: The authors declare no conflict of interest.

References

1. Moxon, T.; Palyanova, G. Agate Genesis: A Continuing Enigma. *Minerals* **2020**, *10*, 953. [[CrossRef](#)]
2. Götze, J.; Möckel, R.; Pan, Y. Mineralogy, geochemistry and genesis of agate—A review. *Minerals* **2020**, *10*, 1037. [[CrossRef](#)]
3. Götze, J.; Tichomirowa, M.; Fuchs, H.; Pilot, J.; Sharp, Z.D. Geochemistry of agates: A trace element and stable isotope study. *Chem. Geol.* **2001**, *175*, 523–541. [[CrossRef](#)]
4. Pršek, J.; Dumańska-Słowik, M.; Powolny, T.; Natkaniec-Nowak, L.; Tobiła, T.; Zych, D.; Skrepnicka, D. Agates from Western Atlas (Morocco)—Constraints from mineralogical and microtextural characteristics. *Minerals* **2020**, *10*, 198. [[CrossRef](#)]
5. Moxon, T.; Reed, S.J.B. Agate and chalcedony from igneous and sedimentary hosts aged from 13 to 3480 Ma: A cathodoluminescence study. *Miner. Mag.* **2006**, *70*, 485–498. [[CrossRef](#)]

6. Moxon, T.; Nelson, D.R.; Zhang, M. Agate recrystallization: Evidence from samples found in Archaean and Proterozoic host rocks, Western Australia. *Aust. J. Earth Sci.* **2006**, *53*, 235–248. [[CrossRef](#)]
7. Svetova, E.; Svetov, S. Mineralogy and Geochemistry of Agates from Paleoproterozoic Volcanic Rocks of the Karelian Craton, Southeast Fennoscandia (Russia). *Minerals* **2020**, *10*, 1106. [[CrossRef](#)]
8. Svetova, E.N.; Chazhengina, S.Y.; Stepanova, A.V.; Svetov, S.A. Black Agates from Paleoproterozoic Pillow Lavas (Onega Basin, Karelian Craton, NW Russia): Mineralogy and Proposed Origin. *Minerals* **2021**, *11*, 918. [[CrossRef](#)]
9. Polekhovskiy, Y.S.; Punin, Y.O. Agate mineralization in basaltoids of the northeastern Ladoga region, South Karelia. *Geol. Ore Depos.* **2008**, *7*, 642–646. [[CrossRef](#)]
10. Khazov, R.A. Riphean complex. In *Geology of Karelia*; Sokolov, V.A., Kulikov, V.S., Stenar, M.M., Eds.; Nauka: Leningrad, Russia, 1987; 172p. (In Russian)
11. Larin, A.M. Jotnian and post-Jotnian (~1.46 Ga and younger) magmatism. In *Proterozoic Ladoga Structure (Geology, Deep Structure and Mineral Genesis)*; Sharov, N.V., Ed.; Karelian Research Centre RAS: Petrozavodsk, Russia, 2020; pp. 145–147.
12. Kuptsova, A.V.; Khudoley, A.K.; Thomas, D. Geology, alteration system, and uranium metallogenic potential of Pasha–Ladoga Basin, Russia. *Miner. Depos.* **2021**, *56*, 1345–1364. [[CrossRef](#)]
13. Glebovitsky, V.A. (Ed.) *Early Precambrian of the Baltic Shield*; Nauka: St. Petersburg, Russia, 2004. (In Russian)
14. Amelin, Y.V.; Larin, A.M.; Tucker, R.D. Chronology of multiphase emplacement of the Salmi rapakivi granitoid complex, Baltic Shield: Implications for magmatic evolution. *Contrib. Miner. Petrol.* **1997**, *127*, 353–368. [[CrossRef](#)]
15. Larin, A.M. *Rapakivi Granites and Related Rocks*; Nauka: St. Petersburg, Russia, 2011; 402p. (In Russian)
16. Velichkin, V.I.; Kushnerenko, V.K.; Tarasov, N.N.; Andreyeva, O.; Kisileva, G.D.; Krylova, T.L.; Doynikova, O.; Golubev, V.N.; Golovin, V.A. Geology and formation conditions of the Karku unconformity-type deposit in the northern Ladoga region (Russia). *Geol. Ore Depos.* **2005**, *47*, 87–112.
17. Sviridenko, L.P.; Svetov, A.P. *Gabbro-Dolerite Valaam Sill and Geodynamics of Ladoga Lake Basin*; Karelian Research Centre RAS: Petrozavodsk, Russia, 2008; 123p. (In Russian)
18. Kulikov, V.S.; Svetov, S.A.; Slabunov, A.I.; Kulikova, V.V.; Polin, A.K.; Golubev, A.I.; Gorkovets, V.Y.; Ivashchenko, V.I.; Gogolev, M.A. Geological map of Southeastern Fennoscandia (scale 1:750,000): A new approach to map compilation. *Trans. KarRC RAS* **2017**, *2*, 3–41. [[CrossRef](#)]
19. Bogdanov, Y.B.; Savatenkov, V.V.; Ivanikov, V.V.; Frank-Kamenetzkiy, D.A. Isotope age of volcanics of the Salmi Formation. In Proceedings of the II Russian Conference on Isotope Geochronology, Sankt-Petersburg, Russia, 25–27 November 2003.
20. Kuptsova, A.V.; Khudoley, A.K.; Davis, W.; Rainbird, R.H.; Kovach, V.P.; Zagornaya, N.Y. Age and provenances of sandstones from the Riphean Priozersk and Salmi formations in the eastern Pasha–Ladoga Basin (southern margin of the Baltic Shield). *Stratigr. Geol. Correl.* **2011**, *19*, 125–140. [[CrossRef](#)]
21. Rämö, O.T.; Mänttari, I.; Vaasjoki, M.; Upton, B.G.J.; Sviridenko, L.P. Age and significance of Mesoproterozoic CFB magmatism, Ladoga Lake region, NW Russia. In Proceedings of the 2001: GSA Annual Meeting and Exposition Abstracts, Boston, MA, USA, 1–10 November 2001.
22. Svetov, S.A.; Stepanova, A.V.; Chazhengina, S.Y.; Svetova, E.N.; Rybnikova, Z.P.; Mikhailova, A.I.; Paramonov, A.S.; Utitsyna, V.L.; Ekhova, M.V.; Kolodey, B.S. Precision geochemical (ICP–MS, LA–ICP–MS) analysis of rock and mineral composition: The method and accuracy estimation in the case study of Early Precambrian mafic complexes. *Tr. KarRC RAS* **2015**, *7*, 54–73. [[CrossRef](#)]
23. Sun, S.; McDonough, W.F. Chemical and isotopic systematics of oceanic basalts: Implications for mantle composition and processes. *Geol. Soc. Spec. Publ.* **1989**, *42*, 313–345. [[CrossRef](#)]
24. Le Maitre, R.W. *Igneous Rocks: A Classification and Glossary of Terms*, 2nd ed.; Cambridge University Press: Cambridge, UK, 2002; p. 236.
25. Godovikov, A.A.; Ripinen, O.I.; Motorin, S.G. *Agates*; Nedra: Moscow, Russia, 1987; p. 368. (In Russian)
26. De Faria, D.L.A.; Venâncio, S.S.; de Oliveira, M.T. Raman microspectroscopy of some iron oxides and oxyhydroxides. *J. Raman Spectrosc.* **1997**, *28*, 873–878. [[CrossRef](#)]
27. Krolop, P.; Jantschke, A.; Gilbricht, S.; Niiranen, K.; Seifert, T. Mineralogical Imaging for Characterization of the Per Geijer Apatite Iron Ores in the Kiruna District, Northern Sweden: A Comparative Study of Mineral Liberation Analysis and Raman Imaging. *Minerals* **2019**, *9*, 544. [[CrossRef](#)]
28. Post, J.E.; McKeown, D.A.; Heaney, P.J. Raman spectroscopy study of manganese oxides: Tunnel structures. *Am. Miner.* **2020**, *105*, 1175–1190. [[CrossRef](#)]
29. Buzgar, N.; Buzatu, A.; Sanislav, I.V. The Raman study on certain sulfates. *Ann. Stiintifice Ale Univ.* **2009**, *55*, 5–23.
30. Zhou, L.; Mernagh, T.P.; Mo, B.; Wang, L.; Zhang, S.; Wang, C. Raman Study of Barite and Celestine at Various Temperatures. *Minerals* **2020**, *10*, 260. [[CrossRef](#)]
31. Wang, A.; Freeman, J.J.; Jolliff, B.L. Understanding the Raman spectral features of phyllosilicates. *J. Raman Spectrosc.* **2015**, *46*, 829–845. [[CrossRef](#)]
32. Arbiol, C.; Layne, G.D. Raman Spectroscopy Coupled with Reflectance Spectroscopy as a Tool for the Characterization of Key Hydrothermal Alteration Minerals in Epithermal Au–Ag Systems: Utility and Implications for Mineral Exploration. *Appl. Spectrosc.* **2021**, *75*, 1475–1496. [[CrossRef](#)] [[PubMed](#)]
33. Zane, A.; Weiss, Z. A procedure for classifying rock-forming chlorites based on microprobe data. *Rend. Lincei* **1998**, *9*, 51–56. [[CrossRef](#)]

34. Hey, M.H. A new review of the chlorites. *Miner. Mag. J. Miner. Soc.* **1954**, *30*, 277–292. [[CrossRef](#)]
35. Shao, Y.; Yan, D.; Qiu, L.; Mu, H.; Zhang, Y. Late Permian High-Ti and Low-Ti Basalts in the Songpan–Ganzi Terrane: Continental Breakup of the Western Margin of the South China Block. *Minerals* **2022**, *12*, 1391. [[CrossRef](#)]
36. Giuliani, A.; Phillips, D.; Kamenetsky, V.S.; Fiorentini, M.L.; Farquhar, J.; Kendrick, M.A. Stable isotope (C, O, S) compositions of volatile-rich minerals in kimberlites: A review. *Chem. Geol.* **2014**, *374–375*, 61–83. [[CrossRef](#)]
37. Valley, J.W. Stable isotope geochemistry of metamorphic rocks. *Rev. Miner. Geochem.* **1986**, *16*, 445–489.
38. Hou, Z.Q.; Griffin, W.L.; Zheng, Y.C.; Wang, T.; Guo, Z.; Hou, J.; Santosh, M.; O'Reilly, S.Y. Cenozoic lithospheric architecture and metallogensis in Southeastern Tibet. *Earth-Sci. Rev.* **2021**, *214*, 103472. [[CrossRef](#)]
39. Moxon, T.; Carpenter, M.A. Crystallite growth kinetics in nanocrystalline quartz (agate and chalcedony). *Miner. Mag.* **2009**, *73*, 551–568. [[CrossRef](#)]
40. Götze, J.; Möckel, R.; Vennemann, T.; Müller, A. Origin and geochemistry of agates from Permian volcanic rocks of the Sub-Erzgebirge basin (Saxony, Germany). *Chem. Geol.* **2016**, *428*, 77–91. [[CrossRef](#)]
41. Powolny, T.; Dumańska-Słowik, M.; Sikorska-Jaworowska, M.; Wójcik-Bania, M. Agate mineralization in spilitized Permian volcanics from “Borówno” quarry (Lower Silesia, Poland)—Microtextural, mineralogical, and geochemical constraints. *Ore Geol. Rev.* **2019**, *114*, 103–130. [[CrossRef](#)]
42. Natkaniec-Nowak, L.; Dumańska-Słowik, M.; Pršek, J.; Lankosz, M.; Wróbel, P.; Gawel, A.; Kowalczyk, J.; Kocemba, J. Agates from Kerrouchen (The Atlas Mountains, Morocco). *Minerals* **2016**, *6*, 77. [[CrossRef](#)]
43. Zhang, X.; Ji, L.; He, X. Gemological characteristics and origin of the Zhanguohong agate from Beipiao, Liaoning province, China: A combined microscopic, X-ray diffraction, and Raman spectroscopic study. *Minerals* **2020**, *10*, 401. [[CrossRef](#)]
44. Götze, J.; Möckel, R.; Kempe, U.; Kapitonov, I.; Vennemann, T. Origin and characteristics of agates in sedimentary rocks from the Dryhead area, Montana/USA. *Miner. Mag.* **2009**, *73*, 673–690.
45. Goncharov, V.I.; Gorodinsky, M.E.; Pavlov, G.F.; Savva, N.E.; Fadeev, A.P.; Vartanov, V.V.; Gunchenko, E.V. *Chalcedony of North-East of the USSR*; Science: Moscow, Russia, 1987; p. 192. (In Russian)
46. Cathelineau, M. Cation site occupancy in chlorites and illites as a function of temperature. *Clay Miner.* **1988**, *23*, 471–485. [[CrossRef](#)]
47. Kranidiotis, P.; MacLean, W.H. Systematics of chlorite alteration at the Phelps Dodge massive sulfide deposit, Matagami, Quebec. *Econ. Geol.* **1987**, *82*, 1898–1911. [[CrossRef](#)]
48. Zang, W.; Fyfe, W.S. Chloritization of the hydrothermally altered bedrocks at the Igarapé Bahia gold deposit, Carajás, Brazil. *Miner. Depos.* **1995**, *30*, 30–38. [[CrossRef](#)]
49. Geptner, A.R. Hydrothermal mineralization in the Iceland rift zone (tectonic control of the formation of mineral concentrations). *Lithol. Miner. Res.* **2009**, *44*, 205–228. [[CrossRef](#)]
50. Mockel, R.; Götze, J.; Sergeev, S.A.; Kapitonov, I.N.; Adamskaya, E.V.; Goltsin, N.A.; Ennemann, T. Trace-Element Analysis by Laser Ablation Inductively Coupled Plasma Mass Spectrometry (LA-ICP-MS): A Case Study for Agates from Nowy Kościół, Poland. *J. Sib. Fed. Univ. Eng. Technol.* **2009**, *2*, 123–138.
51. Conte, A.; Della Ventura, G.; Rondeau, B.; Romani, M.; Cestelli Guidi, M.; La, C.; Napoleoni, C.; Lucci, F. Hydrothermal genesis and growth of the banded agates from the Allumiere-Tolfa volcanic district (Latium, Italy). *Phys Chem Miner.* **2022**, *49*, 39. [[CrossRef](#)]
52. Rollinson, H.; Pease, V. *Using Geochemical Data to Understand Geological Processes*; University Printing House: Cambridge, UK, 2021; 661p.
53. Muller, A.; Herklotz, G.; Giegling, H. Chemistry of quartz related to the Zinnwald/Cinovec Sn-W-Li greisen-type deposit, Eastern Erzgebirge, Germany. *J. Geochem. Explor.* **2018**, *190*, 357–373. [[CrossRef](#)]
54. Svetova, E.N.; Svetov, S.A. Agates from Paleoproterozoic volcanic rocks of the Onega Structure, Central Karelia. *Geol. Ore Depos.* **2020**, *62*, 669–681. [[CrossRef](#)]

Disclaimer/Publisher’s Note: The statements, opinions and data contained in all publications are solely those of the individual author(s) and contributor(s) and not of MDPI and/or the editor(s). MDPI and/or the editor(s) disclaim responsibility for any injury to people or property resulting from any ideas, methods, instructions or products referred to in the content.